European Journal of Medicinal Chemistry 312 (2026) 118838

Contents lists available at ScienceDirect

European Journal of Medicinal Chemistry

journal homepage: www.elsevier.com/locate/ejmech

Research paper

Discovery of APO-50815, a potent WEE1 kinase inhibitor with exceptional efficacy against patient-derived colorectal cancer organoids

Joel L. Syphers [a,1], Josephine A. Wright [b,1], Rebekah de Nys [c], Tharindie N. Silva [c], Laura Vrbanac [c], Kate R. Barratt [c], Julia Leeflang [c], Sadia T. Hasan [c], Sophie F. Thomson [c], Adarsh Kumar [d,e], Andreas Krämer [d,e], Christopher Lenz [d,e], Yi Sing Gee [a], Aeson Chang [a], Savannah Young [a], Erica K. Sloan [a], Stefan Knapp [d,e,f], Daniel L. Worthley [g], Siddhartha Mukherjee [h,i], Kieran Stockton [a], Daniel L. Priebbenow [a,*], Susan L. Woods [b,c,**], Jonathan B. Baell [a,i,***]

[a] Monash Institute of Pharmaceutical Sciences, Monash University, 381 Royal Parade, Parkville, VIC, 3052, Australia
[b] Precision Cancer Medicine Theme, South Australian Health and Medical Research Institute, Adelaide, SA, 5000, Australia
[c] Adelaide Medical School, Adelaide University, Adelaide, SA, 5000, Australia
[d] Institute of Pharmaceutical Chemistry, Goethe University, Max-von-Laue-Str. 9, Frankfurt am Main, 60438, Germany
[e] Structural Genomics Consortium (SGC), Buchmann Institute for Life Sciences, Max-von-Laue-Str. 15, Frankfurt am Main, 60438, Germany
[f] German Translational Cancer Network (DKTK) Site Frankfurt Mainz, Heidelberg, 60590, Germany
[g] Colonoscopy Clinic, Spring Hill, QLD, 4000, Australia
[h] Department of Medicine, Columbia University Medical Center, New York, NY, 10032, USA
[i] Manas AI, New York, NY, 10011, USA

ARTICLE INFO

Keywords:
Colorectal cancer
Metastatic colorectal cancer
Patient-derived organoids
WEE1 kinase
Cell cycle checkpoint
WEE1 inhibitors
Tool compound
Cancer treatment

ABSTRACT

Herein, we report the discovery of APO-50815 (**14**), a potent and selective thietane-3-ol WEE1 inhibitor. When tested against *TP53*-mutated colorectal cancer (CRC) patient-derived organoids (PDOs) grown from peritoneal and liver metastases, **14** exhibited outstanding anticancer efficacy, surpassing previously reported branched alkane counterpart **3**, as well as clinical candidates AZD1775 (**1**) and ZN-c3 (**2**). Against primary CRC organoids with diverse *TP53*, *BRAF* and *KRAS* mutation profiles compared with patient-matched normal colon organoids, **14** exhibited selectively potent activity, yielding exceptionally high TI values (129–238) that highlight a substantial therapeutic window for potential cancer treatment. Against primary CRC PDOs (*TP53*-WT, *BRAF-V600E*, *KRAS*-WT), **14** profoundly elevated DNA damage and replication stress compared to **1**, while amplifying cellular apoptosis, confirming a broadly similar but superior mode of action. Owing to its highly selective and exemplary anticancer efficacy, **14** represents a valuable tool compound for drug testing investigations against primary and metastatic CRCs, especially in the context of PDOs.

* Corresponding author. Monash Institute of Pharmaceutical Sciences, Monash University, 381 Royal Parade, Parkville, VIC, 3052, Australia.
** Corresponding author. Precision Cancer Medicine Theme, South Australian Health and Medical Research Institute, Adelaide, SA, 5000, Australia.
*** Corresponding author. Monash Institute of Pharmaceutical Sciences, Monash University, 381 Royal Parade, Parkville, VIC, 3052, Australia.
E-mail addresses: joel@manasai.co (J.L. Syphers), Josephine.Wright@sahmri.com (J.A. Wright), Rebekah.DeNys@sahmri.com (R. de Nys), franciscohettige.silva@adelaide.edu.au (T.N. Silva), laura.vrbanac@adelaide.edu.au (L. Vrbanac), kate.barratt@sahmri.com (K.R. Barratt), julia.leeflang@adelaide.edu.au (J. Leeflang), sadiatasnim.hasan@adelaide.edu.au (S.T. Hasan), thomsoso@tcd.ie (S.F. Thomson), Kumar@pharmchem.uni-frankfurt.de (A. Kumar), kraemer@pharmchem.uni-frankfurt.de (A. Krämer), Lenz@pharmchem.uni-frankfurt.de (C. Lenz), yising.gee@monash.edu (Y.S. Gee), aeson.chang@monash.edu (A. Chang), savannah.young1@monash.edu (S. Young), Erica.sloan@monash.edu (E.K. Sloan), knapp@pharmchem.uni-frankfurt.de (S. Knapp), dan@colonoscopyclinic.com.au (D.L. Worthley), sm3252@cumc.columbia.edu (S. Mukherjee), Kieran.stockton@monash.edu (K. Stockton), Daniel.Priebbenow@monash.edu (D.L. Priebbenow), susan.woods@adelaide.edu.au (S.L. Woods), jbaell29@gmail.com (J.B. Baell).
[1] First authors: Joel L. Syphers and Josephine A. Wright.

https://doi.org/10.1016/j.ejmech.2026.118838
Received 28 December 2025; Received in revised form 17 March 2026; Accepted 2 April 2026
Available online 5 April 2026
0223-5234/© 2026 The Authors. Published by Elsevier Masson SAS. This is an open access article under the CC BY license (http://creativecommons.org/licenses/by/4.0/).

1. Introduction

The nuclear serine/threonine kinase, WEE1, regulates cell-cycle progression by inhibiting cyclin-dependent kinases CDK1 (CDC2) and CDK2 through inhibitory phosphorylation (Fig. 1) [1–5]. These kinases are essential for progression through the G2/M and S phases of the cell cycle, respectively, and their activity is tightly regulated by DNA-damage repair checkpoints (DDRCs) that function to locate and repair damaged DNA [2,6].

At the G2/M checkpoint, DNA damage activates the ATR-CHK1 signaling pathway, resulting in CHK1-mediated activation of WEE1. The activated WEE1 phosphorylates CDK1 at Y15, inactivating the CDK1-cyclin B complex and inducing G2 phase cell cycle arrest [2,4–7]. This allows time for DNA repair to occur before cell cycle progression into mitosis [2,4–7]. CDK1 activity is counterbalanced by the CDC25 phosphatase, which removes inhibitory phosphorylation, while membrane-associated tyrosine- and threonine-specific CDC2-inhibitory kinase (PKMYT1) provides complementary inhibition of CDK1 via phosphorylation at T14, and to a lesser extent, Y15 [2,4–7]. Notably, PKMYT1 is also a promising drug target in oncology [2].

As cells enter mitosis, WEE1 activity is rapidly suppressed to promote CDK1 activity. Polo-like kinase 1 (PLK1) deactivates WEE1 via phosphorylation, while a double-negative feedback regulatory loop between CDK1 and WEE1 reinforces mitotic entry [2]. In addition, AKT-mediated phosphorylation of WEE1 promotes nuclear export, effectively suppressing WEE1-dependent G2/M arrest enabling progression into mitosis. During mitotic exit, dephosphorylation of WEE1 restores balanced regulation of CDK1 activity, required for cytoskeletal remodeling [2].

Beyond its role at the G2/M checkpoint, WEE1 is a key regulator of the intra-S DDRC and is critical for maintaining DNA replication homeostasis [2]. By modulating CDK1 and CDK2 activity, WEE1 prevents unscheduled replication origin firing, facilitates the repair of stalled replication forks, and maintains nucleotide availability during DNA synthesis [2,8,9]. In addition to its checkpoint functions, WEE1 has been implicated in broader cellular processes, including epigenetic regulation and tumor immune signaling, suggesting roles beyond direct cell-cycle control [2]. Collectively, these activities establish WEE1 as a central regulator of cellular homeostasis [2,4,5].

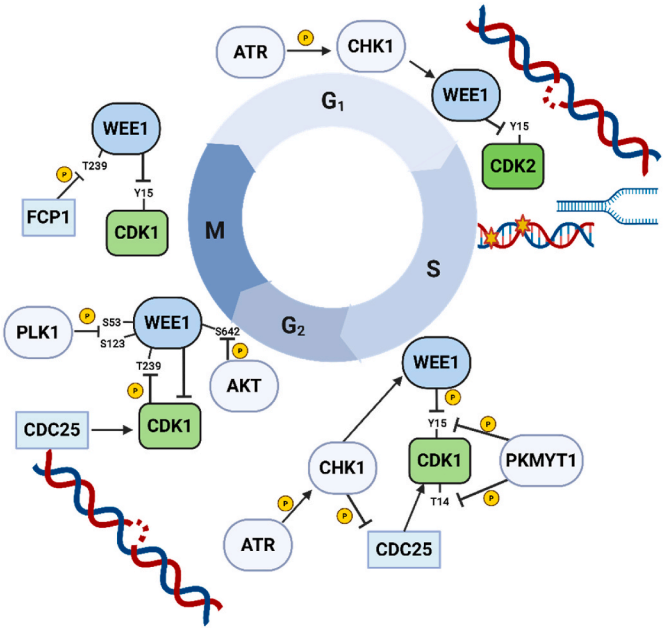

Fig. 1. An overview of the key regulatory proteins of the intra-S and G2/M DDRCs, highlighting the role of WEE1 kinase. Yellow circles with P represent phosphate groups. Arrows represent protein activation due to the addition or removal of a phosphate group. T-shaped arrows represent protein deactivation due to the addition or removal of a phosphate group. (For interpretation of the references to color in this figure legend, the reader is referred to the Web version of this article.)

Given its importance in the intra-S and G2/M DDRCs, WEE1 has emerged as an attractive target for anticancer therapy, particularly in tumors that bear defective G1/S checkpoints due to TP53 mutations [10–12]. Pharmacological inhibition of WEE1 induces replication stress, promotes premature mitotic entry, and triggers mitotic catastrophe in cancer cells [2,4,5,13,14]. Importantly, small molecule WEE1 inhibitors can sensitize tumors to radiotherapy and chemotherapeutic agents, while normal cells retain relative protection through an intact G1/S DNA-damage checkpoint [2,7,15,16].

The pyrimidinylpyrazolone, AZD1775 (adavosertib, **1**) is a potent ATP-competitive inhibitor of WEE1 and was the frontrunner clinical candidate in the past decade (structure of **1** shown in Fig. 2A) [16,17]. Although being considered as generally selective with respect to kinase inhibitors, **1** equally inhibits PLK1, another key regulator of the G2/M DDRC (*vide supra*) [18]. During numerous clinical trials, increased cases of grade 3/4 hematological diseases such as neutropenia and thrombocytopenia were observed with patients treated with **1** [19]. Therefore, it was speculated that the potent PLK1 inhibition of **1** may have caused these adverse events because PLK1 inhibitors in the clinic have also been reported to cause such myelosuppressive diseases [20–23]. However, in 2023 highly selective WEE1 inhibitors were reported to induce thrombocytopenia *in vitro*, therefore the clinical toxicity of **1** was proposed to in fact be as a result of on-target effects, independent of the off-target PLK1 [24]. After completing numerous Phase 2 clinical trials such as for the treatment of metastatic colorectal cancer (mCRC) with mutated *TP53* and *RAS* [25], as well as breast and lung cancers, **1** was discontinued by AstraZeneca primarily due to observed patient tolerability issues in the clinic [19].

In 2021, Zentalis discovered ZN-c3 (azenosertib, **2**), a potent pyrimidinylpyrazolone WEE1 inhibitor clinical candidate derived from the structure of **1**, which demonstrated enhanced selectivity for WEE1 over PLK1 and an improved kinome selectivity profile [26]. In monotherapy, Zentalis plans a Phase 3 randomized confirmatory study with **2** for the treatment of patients with cyclin E1-positive platinum-resistant ovarian cancer [27]. Additionally, in collaboration with Pfizer, **2** was being evaluated in a Phase 1/2 clinical trial with encorafenib and cetuximab for the treatment of patients with *BRAF-V600E*-mutated mCRC. However, this trial has been terminated due to a change in therapeutic landscape [28]. The structural advancement of **2** compared to **1** is its chiral cyclic alcohol moiety extended from the pyridyl ring (structure of **2** shown in Fig. 2A), indicating that pyridyl ring modifications of **1** could result in more potent and selective WEE1 inhibitors [26]. However, the clinical data of **2** is minimal, especially with respect to information on its toxicity profile. Nonetheless, myelosuppressive clinical toxicities have also been reported in patients, albeit to a lesser extent than **1** [29].

Currently no WEE1 inhibitor has been approved by regulatory bodies around the globe, though many are currently being trialed clinically (example drugs are shown in Fig. 2B), and it is unclear what caused the clinical hematological adverse events when patients were treated with **1**. Therefore, there is urgency for the discovery of improved WEE1 inhibitors that exhibit stronger anticancer efficacy than clinical candidates **1** and **2**, which theoretically could be administered at lower doses and potentially alleviate the myelosuppressive toxicities. Building on the discovery of Cmpd **34** (**3**), our previously reported [30] leading WEE1 inhibitor derived from **1** and shown to be more efficacious than both **1** and **2** against patient-derived primary and metastatic CRC organoids, we conducted an SAR investigation of **3**, while simultaneously continuing our SAR analysis of **1** (structure of **3** shown in Fig. 2A). The outcomes of this investigation are described herein, showcasing a new generation of WEE1 inhibitors that have been profiled in our unique patient-derived organoid (PDO) platform for their effects on CRC cell viability.

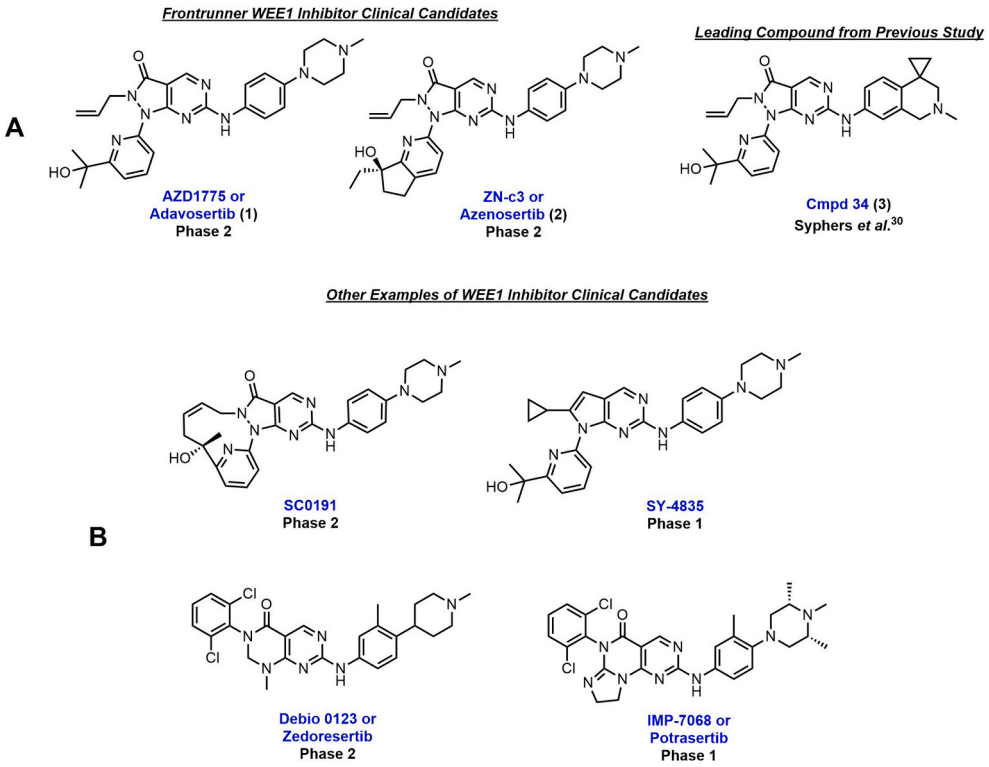

Fig. 2. (**A**) Pyrimidinylpyrazolone-based WEE1 inhibitors, including the anticancer clinical candidates AZD1775 (**1**) and ZN-c3 (**2**), as well as the leading compound (Cmpd **34**, **3**) from our previous study. (**B**) Structures of other WEE1 inhibitor clinical candidates with varying chemotypes.

2. Results and discussion

2.1. Structure-based design strategy

The pyrimidinylpyrazolone core of **3** possesses an isopropyl alcohol-substituted pyridyl ring and an amino cyclopropyl tetrahydroisoquinoline (THIQ) group (Fig. 3A). Computational molecular modelling on the structure of AZD1775 (**1**) bound to WEE1 was evaluated using the ligedit feature of ICM-Pro (version 3.9-4) [31]. The workflow involved preparing the drug-protein complex (PDB ID: 5V5Y, 1.90 Å). Afterward, the ligand and receptor were set up at physiological pH (7.4). Here, the ligedit feature was utilized to modify the *N*-methyl piperazine moiety of the phenyl ring of **1** to the THIQ group of **3**, and after redocking, as well as energy minimization, the theoretical WEE1 binding mode of **3** was analyzed. Key interactions of both **1** and **3** are described in Fig. 3. In brief for both analogues, a hydrogen bond interaction was observed between the hinge region C379 carbonyl and the secondary amine moiety of the phenyl ring, as well as between the amine functionality of the amino acid and a pyrimidine nitrogen atom of the core. In addition, π-π interactions between both F433 and Y378, and both faces of the aromatic pyrimidine moiety were observed, as well as a hydrogen bond interaction between the amide moiety of N376 and the carbonyl group of the pyrimidinylpyrazolone core. The *N*-allyl functionality was observed to be positioned in a lipophilic pocket (in between residues V313, A326 and K328). The isopropyl alcohol substituent of the pyridyl ring was extended towards the G-loop region, with no observable interaction between the alcohol moiety and the protein, only the branched alkane interacting across hydrophobic surfaces. Furthermore, the *N*-methyl piperazine in **1** or THIQ in **3** were directed to solvent, however, an additional salt bridge interaction was observed between the ammonium functionality of the THIQ group in **3** and the carboxylate group of D386. This ammonium functionality of the THIQ was also observed to partake in an intramolecular π-cation interaction with the pyridyl ring. These additional interactions likely explain the enhanced WEE1 potency of **3** compared to **1** [30].

In this investigation, two independent SAR studies were conducted on **1** and **3**. Firstly, as the pyridyl ring has been reported to be a tolerable site for functionalization in derivatives of **1** [26,32], it was of interest to undertake an explorative SAR analysis primarily on the pyridyl ring of **3**. This was to assess whether modification of the pyridyl ring and/or it's isopropyl alcohol substituent could result in enhanced potency against WEE1. It was decided to leave the whole THIQ group untouched as it was observed to aid in improving WEE1 potency (*vide supra*). In addition, it was of interest to build on our previous SAR investigation [30] on **1** by primarily modifying the pyridyl ring. As PLK1 is equipotently inhibited by **1**, and this protein has been linked to hematological diseases in patients, all potent WEE1 inhibitors were tested against PLK1 in order to calculate selectivity index (SI) values against WEE1. Taken together, both focus SAR studies were intended to assess positive effects on biochemical WEE1 inhibition, and this was also analyzed in the context of three-dimensional (3D) mCRC efficacy using patient-derived organoids.

Biochemical Kinase Assays. Our focus was SAR around the pyrimidinylpyrazolone scaffold present in both AZD1775 (**1**) and Cmpd **34** (**3**), a term we use throughout for convenience, albeit that the core more technically is best described as 1,2-dihydro-3*H*-pyrazolo[3,4-*d*]pyrimidin-3-one (Table 1).

In terms of WEE1 inhibition, **1** returned a biochemical IC_{50} value of 41 nM, whereas our previous leading analogue **3** was almost 3-fold more active (IC_{50} value of 14 nM) [30]. Firstly focusing on the SAR explorative analysis of **1**, initial studies investigated whether introducing ethyl alcohol moieties at the *meta*-positions of both the pyridyl and phenyl rings (compound **4**) would be tolerated in WEE1 binding. This dual functionalization aimed to probe the binding pocket from both ends simultaneously. However, these modifications caused a two-fold loss in potency (IC_{50} value of 87 nM) compared to **1**, indicating that bulky substituents on both the pyridyl and phenyl rings simultaneously are not well tolerated within the WEE1 active site. In addition, the loss of potency may have been due to the polar alcohol groups likely directing toward solvent, resulting in the slight restriction of favorable WEE1

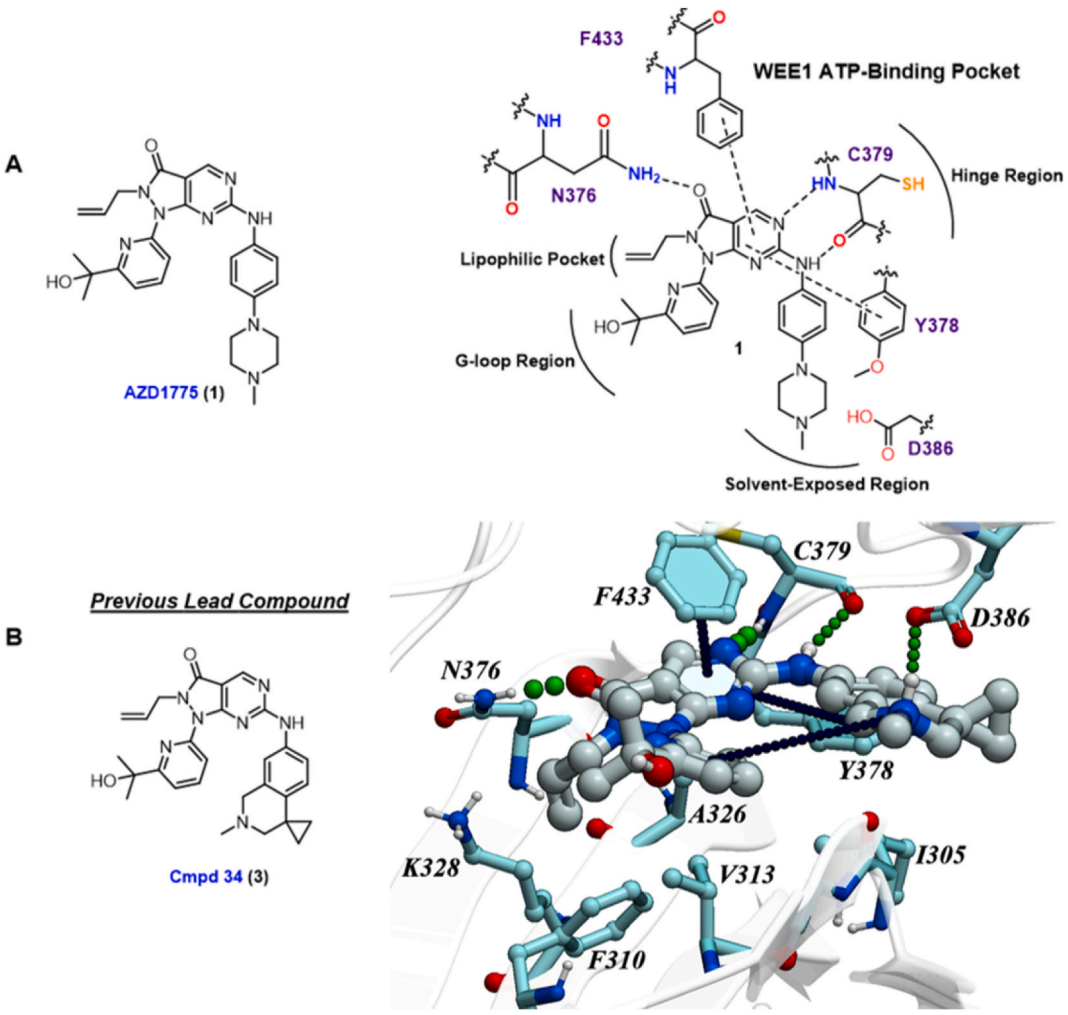

Fig. 3. (**A**) Amino acid residue binding mode of AZD1775 (**1**) with WEE1. (**B**) Computational molecular modeling on an X-ray co-crystal structure (PDB ID: 5V5Y, 1.90 Å) of **1** bound to WEE1, using the ligedit feature of ICM-Pro, to afford Cmpd **34** (**3**), and its binding mode was observed after redocking. This investigation involved SAR analyses of both **1** and **3** for the development of WEE1 inhibitors with improved anticancer efficacy. Green spheres represent hydrogen bond or salt bridge interactions and black spheres represent π-π or π-cation interactions. (For interpretation of the references to color in this figure legend, the reader is referred to the Web version of this article.)

binding of functional groups positioned across hydrophobic regions such as the *N*-allyl and branched alkane groups. Consequently, focus was directed onto only modifying the pyridyl ring of **1**, a site previously reported to tolerate functionalization [32], to assess effects on WEE1 potency.

Rigidifying the branched alkane substituent of the pyridyl ring of **1** to a thietane substantially decreased inhibitory potency, with **5** returning an IC_{50} value of 4900 nM against WEE1. Oxidizing the sulfur atom to the sulfoxide in **6** surprisingly resulted in a profound increase in WEE1 inhibitory potency (IC_{50} value of 16 nM), with improved WEE1 activity compared to **1** and comparable to **3**. Further oxidation to the sulfone moiety in **7** suffered a significant decrease in WEE1 inhibitory potency, returning an IC_{50} value of 1700 nM. These results suggest that intricate modifications of the isopropyl alcohol substituent of the pyridyl ring of **1** may pose a significant role in tight binding of these compounds to WEE1, which is contrary to what was reported previously [32]. Next, it was of interest to assess whether replacing the pyridyl ring of **1** with a thiazol-2-yl in **8** would result in retained WEE1 potency, and fortunately, a WEE1 IC_{50} value of 59 nM was determined.

In terms of PLK1 inhibition, **1** returned an IC_{50} value of 112 nM and a PLK1/WEE1 IC_{50} SI value of 3 was calculated. Incorporation of the two ethyl alcohol groups in **4** returned a significant decrease in PLK1 activity (IC_{50} value of 4800 nM) and consequently an improved SI value of 55 was determined, however, it was noted that **4** was 2-fold less potent against WEE1 than **1**. Next, thietane **5** and sulfone **7** demonstrated significantly decreased activity against PLK1 (IC_{50} values of 9300 and 1100 nM, respectively), but this was analogous to their weak WEE1 inhibitory activity. Encouragingly, the best performing WEE1 inhibitor from this focus set, sulfoxide **6** was significantly less active against PLK1 compared to counterpart **1**, returning an IC_{50} value of 570 nM and a SI value of 36. Furthermore, thiazol-2-yl **8** also demonstrated significantly decreased activity against PLK1 (IC_{50} value of 2000 nM, SI value of 34) compared to **1**.

Next, it was of interest to conduct an explorative SAR analysis on the pyridyl ring of our previous leading analogue **3**. The amino cyclopropyl tetrahydroisoquinoline (THIQ) group was left untouched as molecular modeling and docking studies of **3** against WEE1 demonstrated that the ammonium functionality partook in a salt bridge interaction with the carboxylate group of D386 (see Fig. 3), which likely contributed to the potent activity of **3**. Accordingly, the thiazol-2-yl **9** retained potent WEE1 activity (IC_{50} value of 17 nM) compared to counterpart **3** (IC_{50} value of 59 nM). The thiazol-4-yl regioisomer **10** also retained potent activity, returning an IC_{50} value of 34 nM. Next, the isopropyl alcohol group substituted to the thiazol-4-yl ring of **10** was functionalized to a methyl ether in **11** and modified to a 2-methylprop-1-ene in **12**, and gratifyingly, both analogues returned potent activity against WEE1 (IC_{50}

Table 1
Pyridyl and Phenyl Ring Modification of Pyrimidinylpyrazolone Derivatives, Accompanied with Biochemical Kinase and mCRC PDO Inhibitory Analyses.

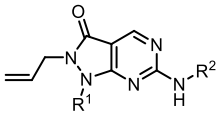

Cmpd[a]	R1	R2	WEE1 IC_{50} (nM)[h]	PLK1 IC_{50} (nM)	SI[b]	PM003[c, g] IC_{50} (nM)	PM025[d, g] IC_{50} (nM)	QEH039LM[e, g] IC_{50} (nM)	QEH042LM[f, g] IC_{50} (nM)
AZD1775 (1)	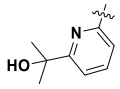	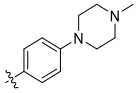	41 ± 1	112 ± 26[h]	3	120 ± 30[j]	290 ± 90[j]	240 ± 120[j]	907 ± 42[j]
ZN-c3 (2)	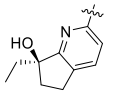	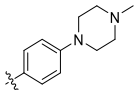				127 ± 33[j]	112 ± 10[j]		
Cmpd 34 (3)	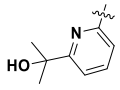	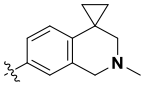	14 ± 3	160 ± 1[h]	12	62 ± 19[j]	80 ± 6[j]	60	
4	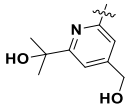	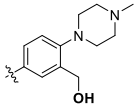	87 ± 2	4800 ± 700[h]	55	77000	29000		
5	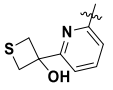	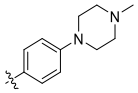	4900 ± 670	9300 ± 350[h]					
6	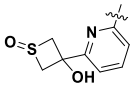	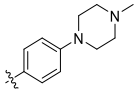	16 ± 1	570 ± 190[h]	36	1000	4000		
7	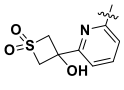	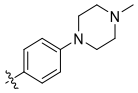	1700 ± 92	7500 ± 1100[h]	4				
8		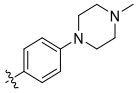	59 ± 28	2000	34	5800	9400		
9		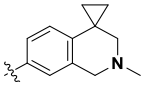	17 ± 1	1000 ± 190[h]	59	730	840		
10		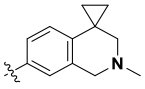	34 ± 4	530 ± 90[h]	16	700	880		
11	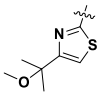	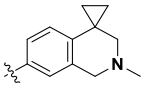	22 ± 8	184 ± 37[h]	8	670	550		
12		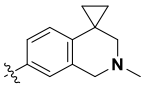	23 ± 8	440 ± 160[h]	19	640	300		
13[i]	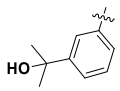	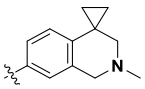	13 ± 3	1300 ± 270[h]	100	98 ± 86[j]	331 ± 170[j]		

(*continued on next page*)

Table 1 (*continued*)

Cmpd[a]	R1	R2	WEE1 IC_{50} (nM)[h]	PLK1 IC_{50} (nM)	SI[b]	PM003[c, g] IC_{50} (nM)	PM025[d, g] IC_{50} (nM)	QEH039LM[e, g] IC_{50} (nM)	QEH042LM[f, g] IC_{50} (nM)
APO-50815 (14)[i]	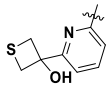	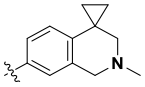	9 ± 2	88 ± 5[h]	10	37 ± 21[j]	74 ± 14[j]	50 ± 7[j]	633 ± 52[j]
15	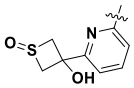	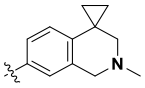	12 ± 2	900	88	7000	3000		
16	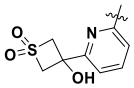	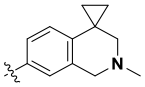	12 ± 3	300	32	350	930		

[a] A series of pyrimidinylpyrazolone compounds were synthesized based on either AZD1775 (**1**) or our previous leading analogue, Cmpd **34** (**3**).
[b] SI refers to selectivity index, the PLK1/WEE1 IC_{50} ratio determined for comparison against **1** and **3**.
[c] PM003 is a PDO line established from peritoneal metastatic CRC tissue.
[d] PM025 is a PDO line established from peritoneal metastatic CRC tissue.
[e] QEH039LM is a PDO line established from liver metastatic CRC tissue.
[f] QEH042LM is a PDO line established from liver metastatic CRC tissue determined to be relatively resistant to treatment with WEE1 inhibitors compared to other CRC PDO lines in this investigation.
[g] PDOs were grown for 2 days and then treated with 7 doses of WEE1 inhibitor in quadruplicate for 5 days, cell viability was assessed via Cell Titer-Glo® assays and IC_{50} values were calculated via nonlinear regression.
[h] Biochemical kinase IC_{50} values that represent the mean of at least two experiments with ±SD (standard deviation).
[i] These compounds were inactive against CHK1 (IC_{50} values of >10 μM).
[j] This symbol refers to mCRC PDO viability assay IC_{50} values that represent the mean of at least two experiments each conducted in quadruplicate with ±SD.

values of 22 and 23 nM, respectively), comparable to **3**. Additionally, as the pyridyl nitrogen of **3** was not observed to partake in any residue interactions during the docking study (see Fig. 3), it was also of interest to determine whether a phenyl counterpart could exhibit potent WEE1 activity. Gratifyingly, **13** retained strong potency (IC_{50} value of 13 nM), comparable to **3**. Shifting focus to the rigidification of the branched alkane of **3** to assess effects on WEE1 potency, thietane (**14**, APO-50815), sulfoxide **15** and sulfone **16**, all exhibited potent activity against WEE1, returning IC_{50} values of 9, 12 and 12 nM, respectively. All of which demonstrated comparably strong WEE1 inhibitory potency to our previous leading analogue **3**.

In terms of PLK1 inhibition, a significant increase in WEE1 selectivity over PLK1 was reported with **3** (IC_{50} value of 160 nM, SI value of 12) compared to **1** [30]. In replacing the pyridyl ring of **3** with a thiazol-2-yl in **9** and thiazol-4-yl in **10**, a significant decrease in PLK1 activity was determined, returning IC_{50} values of 1000 and 530 nM, respectively, as well as respective SI values of 59 and 16. The methyl ester **11** thiazol-4-yl derivative demonstrated enhanced PLK1 activity compared to the isopropyl alcohol-containing counterpart **10**, returning an IC_{50} value of 184 nM and a SI value of 8. Whereas alkene **12** thiazol-4-yl derivative retained decreased PLK1 activity (IC_{50} value of 440 nM, SI value of 19), comparable to **3**. Surprisingly, the phenyl derivative **13** was significantly less active against PLK1 than pyridyl counterpart **3** (IC_{50} value of 160 nM, SI value of 12), returning an IC_{50} value of 1300 nM and a greater SI value of 100. This indicated a purported role of the pyridine nitrogen atom in **3** for adopting a favored bioactive conformation for PLK1, such as intramolecular hydrogen bonding with the isopropyl alcohol moiety or a hydrogen bond interaction with a residue in the active site. Furthermore, the thietane APO-50815 (**14**) was more active against PLK1 than its sulfoxide **15** and sulfone **16** counterparts, returning IC_{50} values of 88, 900 and 300 nM, respectively, and respective SI values of 10, 88 and 32. Although possessing a slightly higher SI than **3** (SI value of 12), **14** is much more selective than clinical candidate **1** (SI value of **3**).

Taken together, this next generation of WEE1 inhibitors is comprised of two focus sets that involved SAR explorative analyses on AZD1775 (**1**) and our previous leading analogue (Cmpd **34**, **3**). Many compounds from this investigation exhibited stronger biochemical potency against WEE1 compared to both **1** and **3**. In addition, numerous analogues were found to be more selective for WEE1 over PLK1 compared to **1**, and in some cases against **3** as well. Therefore, it was then of interest to profile the potent WEE1 inhibitors for anticancer efficacy using 3D patient-derived organoids grown from CRC tissues.

2.2. *WEE1 inhibitor sensitivity testing using patient-derived colorectal cancer organoids*

CRC is the second leading cause of cancer-related deaths around the world [25,33]. The liver is the most common site of metastasis, affecting approximately 50% of advanced cases, while peritoneal metastasis, though less frequent, carry the poorest survival [34]. Effective treatment options for unresectable CRC remain limited, highlighting a critical unmet need for potent small-molecule anticancer agents to treat advanced CRC [35].

Patient-derived organoids (PDOs) preserve (epi)genetic, phenotypic and behavioral characteristics of the parent tissue in long-term cultures. Drug testing in cancer PDOs has matured to the point that it is considered a highly effective model for fast-tracking drug discovery, with potential to predict patient-treatment responses in the clinic and guide personalized treatment options in the future (Fig. 4) [33,36–39]. Recently, the FDA announced plans to reduce or phase out animal studies for replacement with PDOs and organoid-on-chip models for preclinical drug testing of drug safety and efficacy [40].

WEE1 inhibitors such as **1** have been reported to exert antitumor effects on CRC, especially in cases with mutated *TP53* [41]. In addition, we recently reported on the discovery of a library of potent WEE1 inhibitors derived from **1**, that were tested against our unique metastatic and primary CRC PDO platform to determine their effects on malignant cell viability [26]. The THIQ-containing leading compound **3** from this study was determined to be more efficacious against *TP53*-mutated, peritoneal mCRC PDOs (PM003 and PM025) and liver mCRC PDOs (QEH039LM) (IC_{50} values of 62, 80 and 60 nM, respectively) compared to **1** (IC_{50} values of 120, 290 and 240 nM, respectively, see Table 1).

In this investigation, the best performing WEE1 inhibitors were profiled against our unique mCRC PDO platform, specifically against PM003 and PM025 (peritoneal metastases), to measure anticancer efficacy, determine IC_{50} values and indicate the best performing compounds. Thereafter, the leading compound was then tested against liver

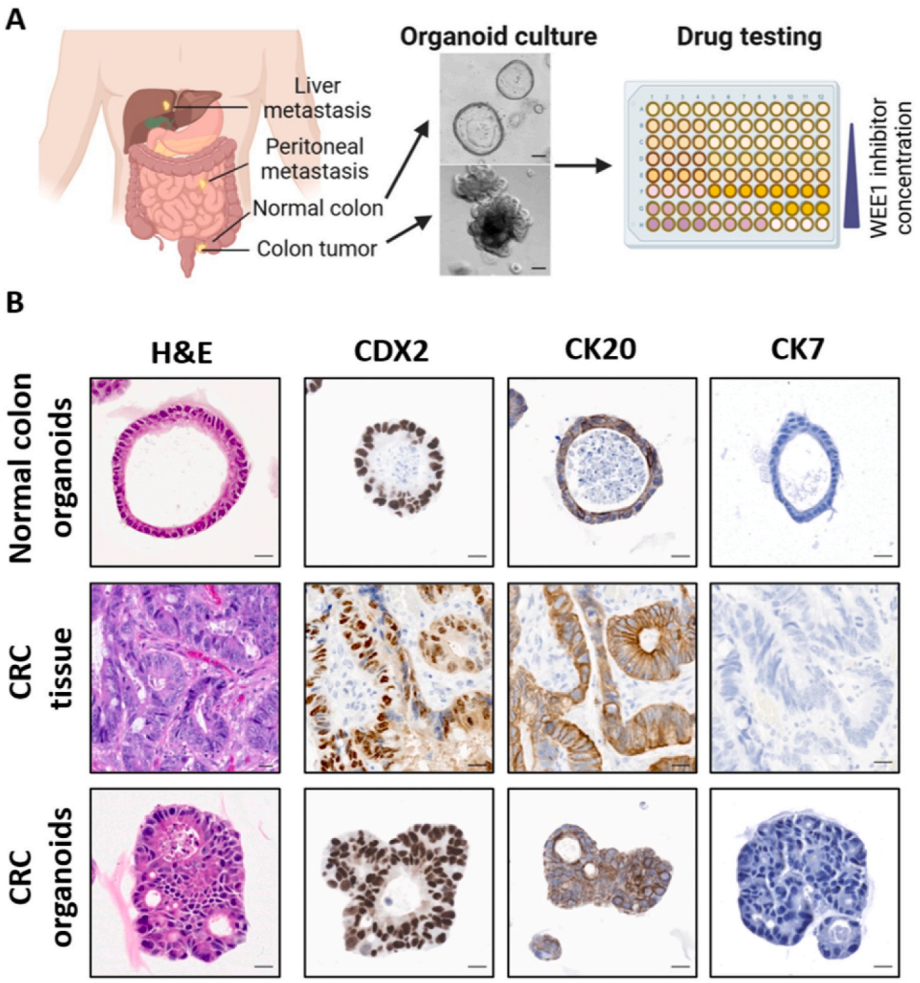

Fig. 4. Primary normal and CRC organoids (novel PDO line RAH057 for example) are representative of the human colon and tumor from which they are derived. (**A**) Schematic illustrating the pipeline from human colorectal cancer (CRC) and normal colon samples to the establishment of patient-derived organoids (PDOs), which are then used for drug testing. (**B**) Organoids are morphologically similar to the native tumor (H&E) and express intestinal epithelial markers, CDX2 and CK20, but not CK7. Scale bar 20 μm (H&E and immunohistochemistry). Scale bar 100 μm (brightfield).

mCRC PDOs, QEH039LM, and QEH042LM (an additional liver mCRC PDO line that was previously characterized in our CADD macrocyclic WEE1 inhibitor study [42], which was found to possess mutated *KRAS,* and was more resistant to treatment with WEE1 inhibitors) in order to further evaluate its effects on malignant cell viability. For more information on the mCRC PDO lines used in this study, in particular patient information and *TP53* (Fig. S1), *BRAF-V600E* and *KRAS* mutation sequencing (Fig. S2), see **Supp**.

Interestingly, diol **4** (WEE1 IC_{50} value of 87 nM) demonstrated significantly decreased activity against PM003 and PM025, returning IC_{50} values of 77000 and 29000 nM, respectively. It was reasoned that these results were likely due to the presence of highly polar ethyl alcohol groups (also as HBDs) in **4** which may have contributed to poor cellular permeability [43]. In addition, the sulfoxide analogue **6** (WEE1 IC_{50} value of 16 nM) also demonstrated poor activity against PM003 and PM025, returning IC_{50} values of 1000 and 4000 nM, respectively, even though it exhibited exceptional biochemical WEE1 potency. Poor cellular permeability was also expected as a major contributor to these results due to the highly polar sulfoxide moiety in **6** [43]. The thiazol-2-yl **8** (WEE1 IC_{50} value of 59 nM) also demonstrated poor malignant organoid inhibitory activity, returning IC_{50} values of 5800 nM against PM003 and 9400 nM against PM025.

Moving focus to the derivatives of our previous leading analogue **3**, encouragingly, a general increase of peritoneal mCRC PDO activity was observed within this focus set. Against PM003 and PM025, the thiazol-2-yl **9** (WEE1 IC_{50} value of 17 nM) demonstrated modest PDO inhibitory activity, returning respective IC_{50} values of 730 and 840 nM. The modest organoid efficacy was retained with thiazol-4-yl **10** (WEE1 IC_{50} value of 34 nM), returning IC_{50} values of 700 nM against PM003 and 880 nM against PM025. The methoxy **11** (WEE1 IC_{50} value of 22 nM) and 2-methylprop-1-ene **12** (WEE1 IC_{50} value of 23 nM) were determined to also exhibit modest activity against the peritoneal metastases, with respective IC_{50} values of 670 and 640 nM against PM003, as well as IC_{50} values of 550 and 300 nM against PM025.

Gratifyingly, the phenyl derivative **13** (WEE1 IC_{50} value of 13 nM) of **3** exhibited strong anticancer efficacy against PM003 (IC_{50} value of 98 nM) and modest activity against PM025 (IC_{50} value of 331 nM), however was found to be less efficacious than **3** (PM003 IC_{50} value of 62 nM and PM025 IC_{50} value of 80 nM). Furthermore, the thietane-3-ol APO-50815 (**14**, WEE1 IC_{50} value 9 nM) was determined to be the strongest anticancer WEE1 inhibitor of this whole series, returning profoundly potent IC_{50} values of 37 and 74 nM against PM003 and PM025, respectively. As expected, although being potent WEE1 inhibitors, the enhanced polarity of counterparts sulfoxide **15** (WEE1 IC_{50} value of 12 nM) and sulfone **16** (WEE1 IC_{50} value of 12 nM), resulted in a significant decrease in organoid efficacy compared to **14**, likely due to challenges in cell permeation [43,44]. Accordingly, sulfoxide **15** returned IC_{50} values of 7000 and 3000 nM against PM003 and PM025, respectively. Sulfone **16** on the other hand demonstrated relatively modest activity against PM003 and PM025, returning IC_{50} values of 350

and 930 nM, respectively.

Taken together, the leading compound from this investigation was the thietane-3-ol-containing THIQ analogue, APO-50815 (**14**), which demonstrated exceptional anticancer efficacy against the peritoneal mCRC PDO lines (PM003 and PM025), and was determined to be approximately 3-fold more active than clinical candidate **1** and almost 2-fold more active than the previous leading compound **3**.

Broadly, the results from testing this series of potent WEE1 inhibitors against the mCRC PDO lines derived from peritoneal metastases demonstrated a wide range of inhibitory activity results, with a number of compounds exhibiting poor efficacy against the PDOs. There are a number of reasons that could explain why some of these compounds were not active in organoids but inhibited purified enzyme biochemically. For example the inability to maintain activity in organoid media due to chemical modifications (such as redox reactions), inability to permeate/transport into cells or being efflux out of cells, modification by other enzymes in cells, the biochemical target was inaccessible in cells, and/or poor physicochemical properties such as high polarity or many HBDs [43,44].

Next, the best-in-class clinical candidate ZN-c3 (**2**), which is scheduled to commence Phase 3 clinical trials, was also tested against the peritoneal *TP53*-mutated mCRC PDO lines (PM003 and PM025) and was reported in our previous study for comparison with our WEE1 inhibitors [30]. In brief, **2** returned potent IC_{50} values of 127 nM and 112 nM, respectively (see Table 1). Gratifyingly, the leading compound from this study, APO-50815 (**14**), exhibited approximately a 3-fold increase in potency compared to clinical candidates **1** and **2**, as well as enhanced potency than the previous leading analogue Cmpd **34** (**3**), highlighting the exceptional anticancer efficacy of **14** against CRC PDOs derived from peritoneal metastases (Fig. 5).

Thereafter, the leading WEE1 inhibitor (APO-50815, **14**) of this investigation was tested against the *TP53*-mutated CRC PDO lines derived from liver metastases and returned an IC_{50} value of 50 nM against QEH039LM and 633 nM against QEH042LM (which also possessed mutated *KRAS*). APO-50815 (**14**) was determined to exhibit stronger anticancer efficacy against QEH039LM and QEH042LM than clinical candidates **1** and **2**, with an almost 5-fold improvement against QEH039LM (IC_{50} values of 240 and 228 nM, respectively) and enhanced activity against the more WEE1 inhibitor-resistant mCRC PDO line QEH042LM (IC_{50} values of 907 and 873 nM, respectively, Fig. 6).

Furthermore, a *TP53*-mutated and *BRAF-V600E* primary CRC organoid line (RAH051T) and a patient-matched normal healthy colon organoid line (RAH051N), characterized in our previous study [30], were treated with the best performing WEE1 inhibitors of this investigation; compound **13** and APO-50815 (**14**), to assess their effects on healthy and malignant cell viability, as well as to measure therapeutic index (TI) values (Fig. 7). Gratifyingly, phenyl analogue **13** returned an IC_{50} value of 5700 nM against RAH051N and 140 nM against RAH051T,

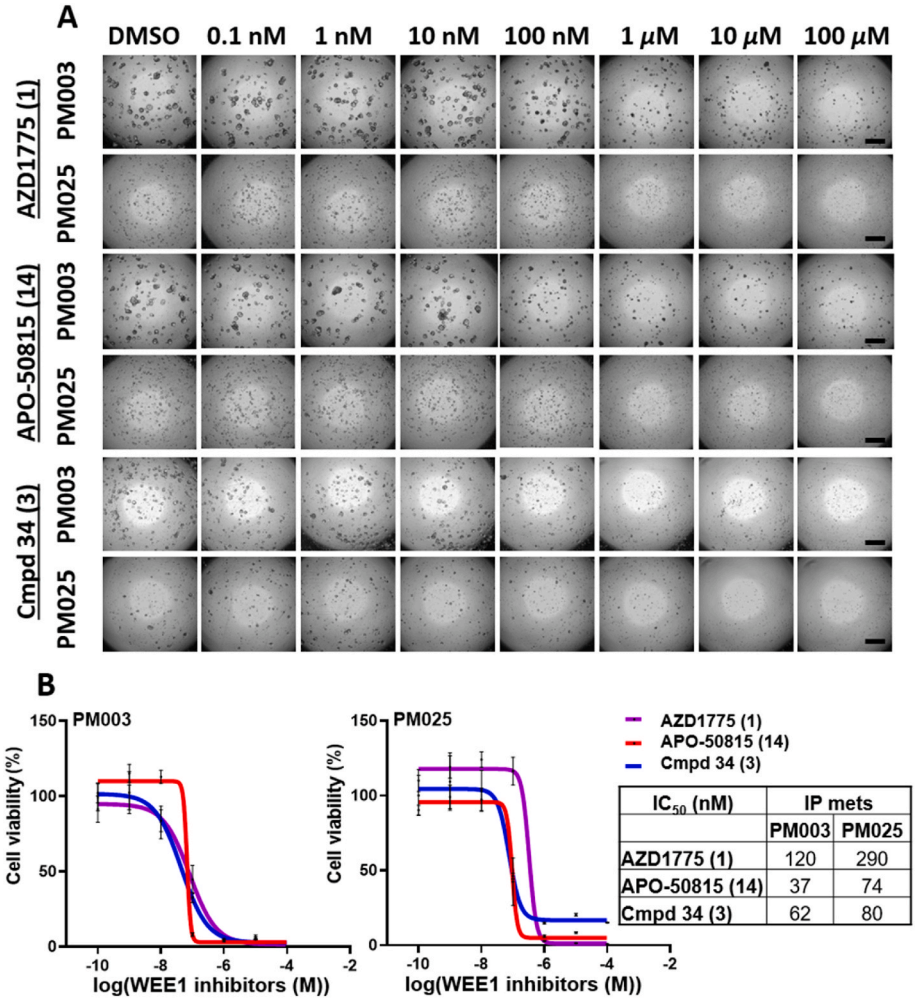

Fig. 5. *TP53*-mutated peritoneal mCRC organoids are sensitive to WEE1 inhibitors. (**A**) Representative images of peritoneal mCRC organoids (PM003 and PM025) treated with WEE1 inhibitors; AZD1775 (**1**), APO-50815 (**14**), Cmpd **34** (**3**). Scale bar 500 μm. (**B**) Representative dose-response curves of PM003 and PM025 organoids treated with WEE1 inhibitors (**1**, **14** and **3**). Organoids were treated in quadruplicate and cell viability was assessed with Cell-Titer Glo assays in at least two independent experiments. Nonlinear regression curve fitting was used to calculate IC_{50} values.

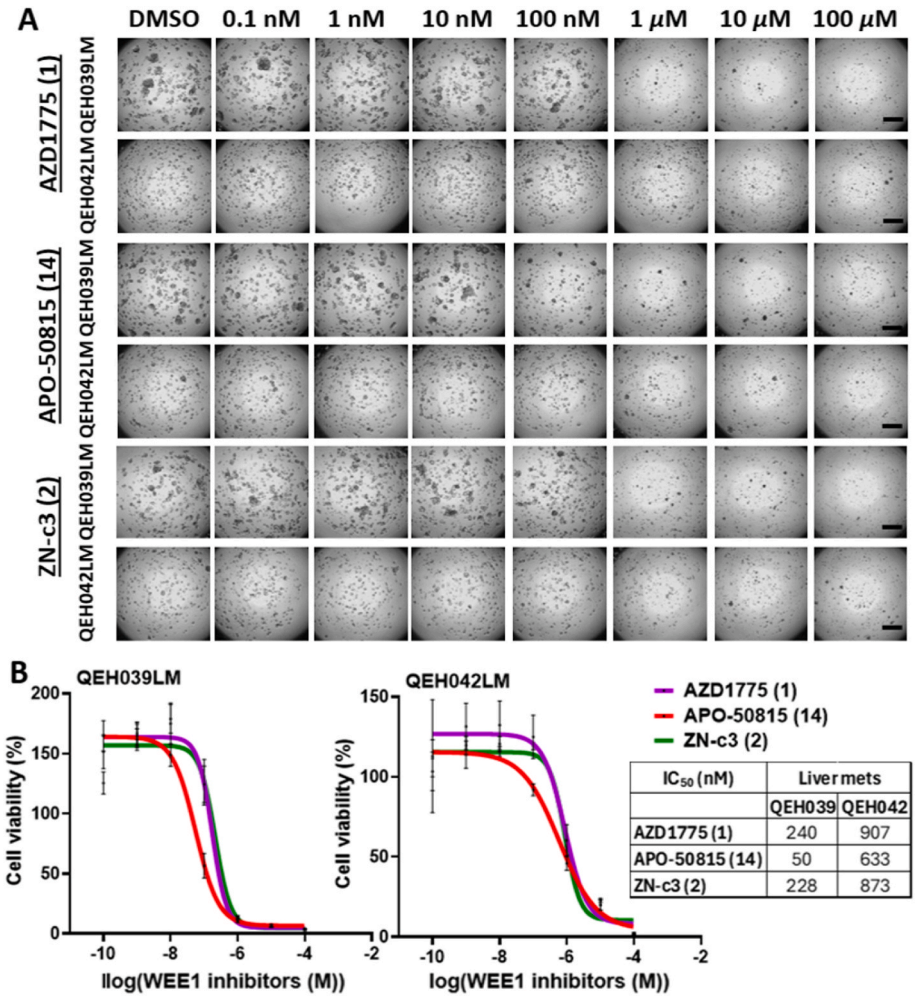

Fig. 6. *TP53*-mutated liver mCRC organoids are sensitive to WEE1 inhibitors. (**A**) Representative images of liver mCRC organoids (QEH039LM and QEH042LM) treated with WEE1 inhibitors; AZD1775 (**1**), APO-50815 (**14**) and ZN-c3 (**2**). Scale bar 500 μm. (**B**) Representative dose-response curves of QEH039LM and QEH042LM organoids treated with WEE1 inhibitors (**1**, **14**, and **2**). Organoids were treated in quadruplicate and cell viability was assessed with Cell-Titer Glo assays in at least two independent experiments. Nonlinear regression curve fitting was used to calculate IC_{50} values.

returning an outstanding TI value of 41. Similarly, APO-50815 (**14**) returned an IC_{50} value of 9300 nM against RAH051N and 39 nM against RAH051T, returning an exceptional TI value of 238. These results demonstrate that WEE1 inhibitors can be significantly more selective at treating primary CRC compared to patient-matched normal colon cells, consistent with what was observed in our previous account [30]. This is because Cmpd **34** (**3**) was also reported to possess a large TI of 20 when treated against RAH051, although significantly lower than both **13** and **14**. It was recognized that both **13** and APO-50815 (**14**) exhibited profoundly selective anticancer efficacy against RAH051T, only demonstrating apoptotic effects on patient-matched healthy cell viability at a high concentration. Taken together, these results not only highlight the potentially favorable safety profile of **13** and **14**, but also showcases its ability to selectively treat *TP53*-WT primary CRC with an intact G1/S DDRC and *BRAF-V600E*.

Building on this success, leading WEE1 inhibitor APO-50815 (**14**) was tested against two additional patient-matched normal colon vs. primary CRC organoid lines; RAH035 (80 y/o male with low grade adenocarcinoma, *TP53*-mutated, *BRAF*-WT and *KRAS*-WT, previously characterized in our CADD macrocyclic WEE1 inhibitor study) [42] and a novel matched PDO line RAH057 (67 y/o female with low grade/-moderately differentiated adenocarcinoma, *TP53*-mutated, *BRAF*-WT and *KRAS*-mutated, histology in Fig. 4, see **Supp** for more information on mutation sequencing). APO-50815 (**14**) returned an IC_{50} value of 6700 nM against RAH035N and 46 nM against RAH035T, with an exceptional TI value of 146. In addition, **14** returned an IC_{50} value of 13000 nM against RAH057N and 101 nM against RAH057T, also with an outstanding TI value of 129 (Fig. 8).

Overall, APO-50815 (**14**) was determined to exhibit profound anticancer activity against the *TP53*-mutated liver (QEH039LM) and peritoneal mCRC PDOs (PM003 and PM025), as well as enhanced activity against the *TP53*-mutated and *KRAS*-mutated liver mCRC PDO line QEH042LM, which was previously determined to be more resistant to treatment with WEE1 inhibitors. Furthermore, **14** demonstrated significant selectivity at potently treating primary CRC PDOs compared to patient-matched normal colon organoids, regardless of *TP53* mutation status, and whether they possess *BRAF-V600E* or mutated *KRAS*.

Next, it was of interest to determine whether the leading WEE1 inhibitor of this study (APO-50815, **14**) broadly drives a similar phenotype as **1**, by inducing DNA damage and replication stress. Therefore, a comparative analysis was conducted measuring active cell cycling, percentage of cells in the S phase, DNA damage and cellular apoptosis, using the *TP53*-mutated and *BRAF-V600E* primary CRC PDO line RAH051T (Fig. 9).

The number of actively cycling cells typically decreases during replication stress, these cells were identified by incorporation of BrdU label into treated CRC organoids following a 3 h pulse of 20 μM BrdU. Concurrently, the % of S phase cells was calculated by analysis of

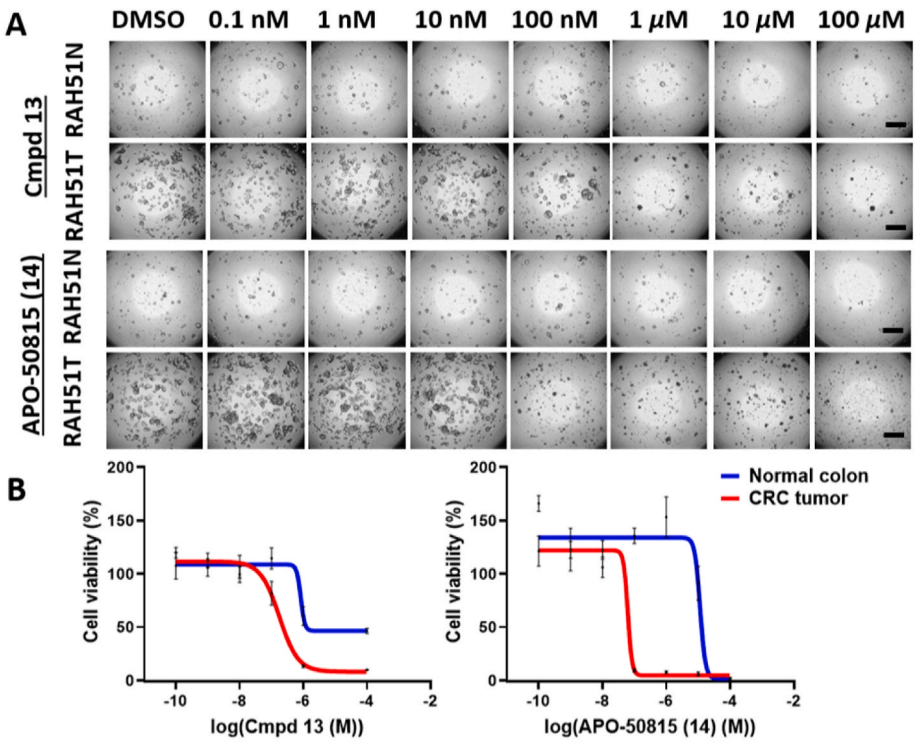

IC_{50} (nM)	Normal colon & primary CRC		
	RAH051N	RAH051T	TI
Cmpd 13	5700	140	41
APO-50815 (14)	9300	39	238

Fig. 7. *TP53*-WT and *BRAF-V600E* primary CRC organoids are significantly more sensitive to WEE1 inhibitors than patient-matched normal colon organoids. (**A**) Representative images of normal human colon (RAH051N) and matched tumor (RAH051T) organoids treated with the best performing WEE1 inhibitors of this study; cmpd **13** and APO-50815 (**14**). Scale bar 500 μm. (**B**) Representative dose-response curves of normal human colon (blue) and matched tumor (red) RAH051 organoids when treated with **13** and **14**. Organoids were treated in quadruplicate and cell viability was assessed with Cell-Titer Glo assays in three independent experiments. Nonlinear regression curve fitting was used to calculate IC_{50} values. (For interpretation of the references to color in this figure legend, the reader is referred to the Web version of this article.)

incorporated DAPI stain. An early response to the induction of double stranded DNA breaks is the phosphorylation of the histone variant H2AX on residue S139, forming ɣH2AX. ɣH2AX functions to recruit and localize DNA-damage reparatory proteins or cell cycle checkpoint factors to damaged DNA sites. Thus, DNA damage was calculated as the percentage of cells labelled with fluorescent antibodies specific for phosphorylated H2AX (pS139) [45]. Poly [ADP-Ribose] Polymerase (PARP) is a nuclear chromatin-associated enzyme that detects and responds to DNA damage. During apoptosis, Caspase-3 cleaves PARP resulting in its inactivation and the inability of cells to repair damaged DNA. Thus, apoptosis was calculated as the percentage of cells containing cleaved PARP using fluorescently labelled antibody specific for cleaved PARP (D214) [14,46].

APO-50815 (**14**) broadly demonstrated a mode of action similar to clinical candidate **1** in inducing DNA damage and replication stress. Both **14** and **1** were found to significantly decrease actively cycling cells compared to the vehicle, though gratifyingly, **14** profoundly intensified DNA damage and the % of cells in the S phase compared to **1**, as well as significantly enhanced cellular apoptosis. It was noted that APO-50815 (**14**) exceptionally augmented approximately >30% more DNA damage than **1** in RAH051T, underscoring its position as a superior WEE1 inhibitor anticancer agent (for more information on the percentage of actively cycling cells following treatment with **14** and **1**, see Fig. S3 in **Supp**).

2.3. Leading WEE1 inhibitors abrogate CDK1 phosphorylation in cells

Biomarker response assays were then performed to measure WEE1 phosphorylation on the Tyr15 (Y15) residue of CDK1 to confirm whether the best performing compounds inhibit WEE1 intracellularly, as well as evaluate if potent anticancer effects on cell viability observed with **13** and APO-50815 (**14**) (*vide supra*) can reasonably be linked to WEE1 target engagement. A human triple negative breast cancer cell line ($MDA\text{-}MB\text{-}231^{HM}$) was chosen as it lacks a G1/S DDRC due to mutated *TP53* and relies on the G2/M and intra-S DDRCs for DNA-damage repair of the malignant cells before mitosis. As WEE1 and CDK1 are key proteins of such DDRCs, $MDA\text{-}MB\text{-}231^{HM}$ constitutively possesses pTyr15-CDK1 [47].

To demonstrate a functional effect of these compounds on WEE1 in a cellular system, the cancer cell lines were treated with approximately 10 × the biochemical WEE1 IC_{50} of **13** and APO-50815 (**14**). In brief, 150 nM of **13** and 90 nM of **14** were used in the assays. The CDK1 and pTyr15-CDK1 protein concentrations were measured via western blotting and the relative concentrations of both proteins were quantitated the WEE1 inhibitors. It was found that both **13** and **14** significantly reduced pTyr15-CDK1 at the chosen concentrations, confirming a functional inhibitory effect of these compounds on WEE1 activity in $MDA\text{-}MB\text{-}231^{HM}$ cancer cells. These results also suggest that **13** and **14** were successful in permeating across cell membranes of $MDA\text{-}MB\text{-}231^{HM}$ to engage with WEE1, which was likely also the case when they were tested against organoids (Fig. 10).

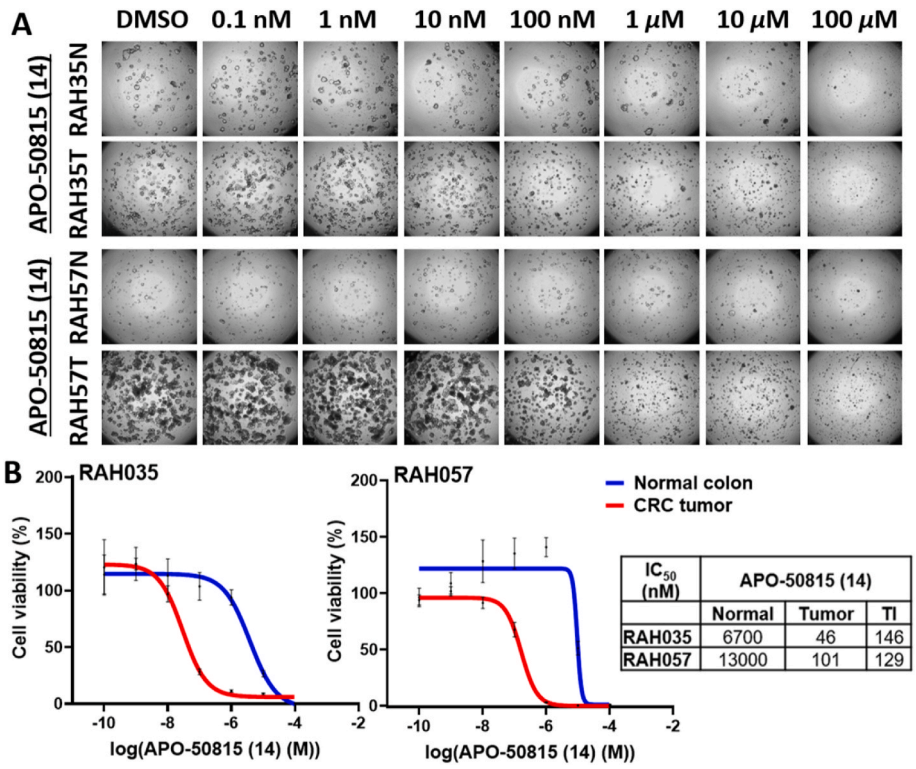

IC_{50} (nM)	APO-50815 (14)		
	Normal	Tumor	TI
RAH035	6700	46	146
RAH057	13000	101	129

Fig. 8. *TP53*-mutated primary CRC organoids are significantly more sensitive to WEE1 inhibitors than patient-matched normal colon organoids. (**A**) Representative images of normal human colon (RAH035N and RAH057N) and matched tumor (RAH035T and RAH057T) organoids treated with APO-50815 (**14**). Scale bar 500 μm. (**B**) Dose-response curves of normal human colon (blue) and matched tumor (red) RAH035 and RAH057 PDO lines. Organoids were treated in quadruplicate and cell viability was assessed with Cell-Titer Glo assays in two independent experiments. Nonlinear regression curve fitting was used to calculate IC_{50} values. (For interpretation of the references to color in this figure legend, the reader is referred to the Web version of this article.)

2.4. *WEE1 inhibitor APO-50815 exhibits kinome-wide selectivity*

To assess the broader kinase selectivity profile of APO-50815 (**14**), the leading compound was tested across a panel of 92 proteins in a thermal shift assay using differential scanning fluorimetry. This was to measure ligand-protein binding via calculating ΔT_m values (for completed data, see Fig. S4 in **Supp**). APO-50815 (**14**) was found to bind tightly with WEE1 ($\Delta T_m = 8.5$ K), which was significantly higher than the reference potent pan-kinase inhibitor staurosporine ($\Delta T_m = 4.5$ K) [48]. Furthermore, the thermal shifts for the closest off-targets ABL1 ($\Delta T_m = 5.7$ K), MAPK15 ($\Delta T_m = 4.7$ K), RPS6KA5 ($\Delta T_m = 4.6$ K) and FLT1 ($\Delta T_m = 4.6$ K) were insignificant compared to their reference compounds, returning respective ΔT_m values of 26, 14, 15.6 and 12 K, which were much larger shifts compared to WEE1 (Fig. 11).

Furthermore, leading compounds (**13** and **14**) were also profiled for biochemical activity against an upstream G2/M checkpoint regulator, CHK1, to further assess kinome-wide selectivity (CHK1 wasn't included in the panel), and gratifyingly, these compounds returned IC_{50} values of >10 μM.

Taken together, APO-50815 (**14**) was found to bind tightly with WEE1 via a thermal shift assay and clearly demonstrated exceptional kinome-wide selectivity.

2.5. *In vitro metabolic evaluation of APO-50815*

Building on the outstanding organoid anticancer efficacy demonstrated by APO-50815 (**14**), negligible toxicity detected in patient-matched normal healthy colon organoids and favorable kinase selectivity profile, it was then of interest to profile **14** against human and mouse liver microsomes *in vitro* to assess the stability of the leading compound (Table 2).

It was determined that the degradation half-lives of **14** in both mouse and human liver microsomes ($T_{1/2} = 4$ and 2 min, respectively) were very short. In addition, respective high intrinsic clearances (CL_{int}) of 326 and 680 μL/min/mg protein, and unbound intrinsic clearances (unbound CL_{int}) of 608 and 1265 μL/min/mg protein, were observed in the mouse and human liver microsomes for **14**. Albeit being an exceptional 2D cellular and 3D organoid anticancer tool compound, these results, overall, reflect pharmacokinetic characteristics of **14** that require future optimization if oral bioavailability is an end-point.

3. Chemistry

The synthetic routes followed to obtain the pyrimidinylpyrazolone analogues of this investigation are displayed below. Firstly, the allyl pyrimidinylpyrazolone building block **16** was synthesized according to a reported procedure [10]. The THIQ intermediate **20** was synthesized according to a procedure reported in our previous study [30]. The thiazole containing WEE1 inhibitors were synthesized according to Scheme 1. An Ullman-type reaction between **16** and, **17** and **10a**–**12a** afforded intermediates **18** and **10b**–**12b**, respectively. Compound **18** was then oxidized and underwent a subsequent S_NAr reaction with either piperazine **19** and THIQ **20** to furnish compounds **8** and **9**, respectively. Next, intermediates **10b**–**12b** were oxidized and then subjected to a S_NAr reaction with **20** to furnish compounds **10**–**12**, respectively. Final compound yields 10–47%.

Next, the synthetic routes followed to obtain compounds **4**, **6**–7 and **13**, **15**–**16** are displayed in Scheme 2. An Ullman-type reaction between **16** and, **4a**, **13a** and **21** afforded intermediates **4b**, **13b** and **22**, respectively. Compound **4b** was then oxidized and underwent a subsequent S_NAr reaction with piperazine **23** to furnish compound **4**. Next, intermediate **22** was oxidized with Oxone® and then subjected to a S_NAr reaction with **19** to afford compound **6**. In addition, **22** was oxidized with *m*-CPBA and then subjected to a S_NAr reaction with **19** to afford

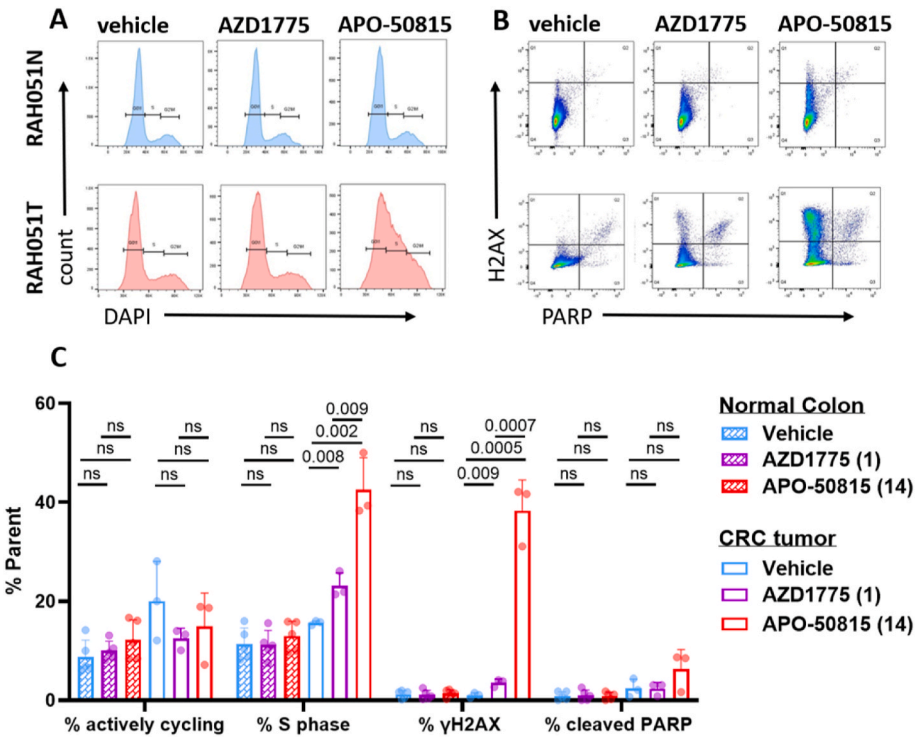

Fig. 9. PDOs derived from matched normal colon (RAH051N) and *TP53*-WT primary CRC tumor (RAH051T) tissues were treated with 300 nM of WEE1 inhibitors (AZD1775 (**1**) and APO-50815 (**14**)) for 48 h before staining using the Apoptosis, DNA Damage and Cell Proliferation Kit (BD Pharmingen) combined with flow cytometric analysis. Actively cycling cells were calculated as the percentage of cells that incorporated BrdU after a 3 h pulse with 20 μM BrdU. S phase cells were detected using DAPI staining (**A**). DNA damage was calculated as the percentage of cells that had phosphorylated H2AX (γH2AX) using the antibody AlexaFluor 647 Mouse Anti H2AX (pS139). Apoptosis was calculated as the percentage of cells that had cleaved PARP using the antibody PE Anti-Cleaved PARP (D214) (**B**). Results are from three independent experiments, *t*-test was used for statistical analysis (**C**).

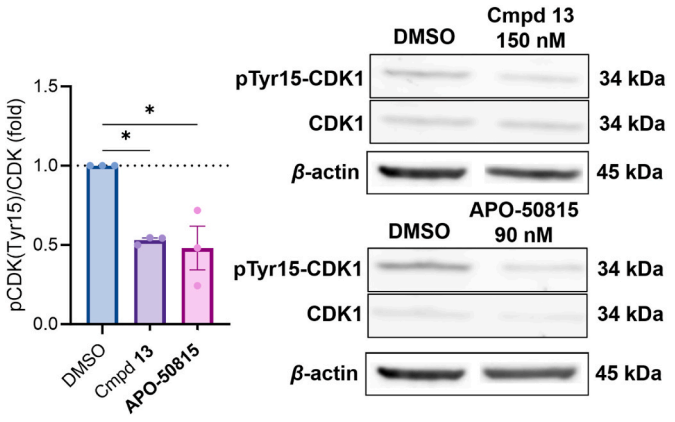

Fig. 10. Western blots demonstrate a significant intracellular decrease of pTyr15-CDK1 concentration due to WEE1 inhibition by compound **13** and APO-50815 (**14**) at approximately 10 × their biochemical WEE1 IC_{50}. Experiments were conducted in a human triple negative breast cancer cell line (MDA-MB-231^{HM}). *β*-Actin as the loading control and DMSO as the vehicle. Bars represent the quantification of the relative pTyr15-CDK1/CDK1. Results are expressed as average values, ±SD ($n = 3$).

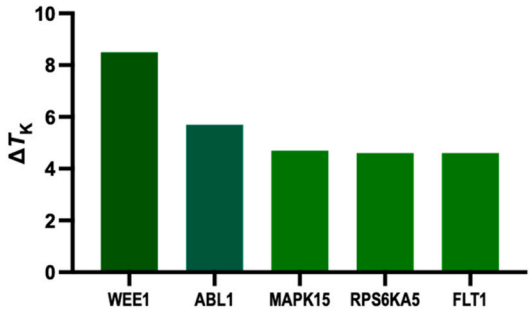

Protein	APO-50815 (ΔT_K)	Reference Compound	Reference (ΔT_K)
WEE1	8.5	Staurosporine	4.5
ABL1	5.7	Ponatinib	26.0
MAPK15	4.7	Staurosporine	14.0
RPS6KA5	4.6	Staurosporine	15.6
FLT1	4.6	Staurosporine	12.0

Fig. 11. Summary of the kinome selectivity profile of leading compound APO-50815 (**14**) via a thermal shift assay.

compound **7**. Intermediate **13b** was oxidized with *m*-CPBA and then underwent a S_NAr reaction with **20** to give compound **13**. Next, **22** was oxidized with Oxone® and then subjected to a S_NAr reaction with **20** to afford compound **15**. Lastly, **22** was oxidized with *m*-CPBA and then underwent a S_NAr reaction with **20** to afford compound **16**. Final compound yields 10–85%.

Thietane analogues **5** and the leading compound APO-50815 (**14**) were obtained following the synthetic route displayed in Scheme 3. Firstly, dibromo intermediate **24** underwent a Li-halide exchange and was quenched with thietane-3-ol to afford **21**. Intermediate **25** was synthesized according to a reported procedure [10]. Compound **25** was oxidized with *m*-CPBA and then underwent a S_NAr reaction with **19** or **20** to afford intermediates **26** and **27**, respectively. An acid-mediated Boc-deprotection reaction of **26** and **27** gave secondary amine intermediates that were treated with base to induce an intramolecular cyclization reaction. Next, an Ullman-type rection between the aforementioned intermediates and **21** furnished **5** and APO-50815 (**14**), respectively. Final compound yields 51–52%.

Table 2
In vitro metabolic evaluation of APO-50815 (**14**).

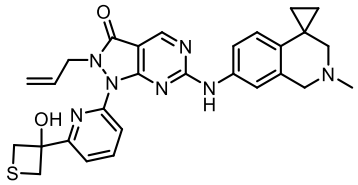

$T_{1/2}$ (min)[a]		CL_{int}[b] ((μL/min)/mg protein)		Unbound CL_{int}[c] ((μL/min)/mg protein)	
mouse	human	mouse	human	mouse	human
4	2	326	680	608	1265

[a] $T_{1/2}$ refers to the degradation half-life in mouse and human liver microsomes.
[b] CL_{int} refers to *in vitro* plasma protein bound intrinsic microsomal clearance.
[c] Unbound CL_{int} refers to *in vitro* plasma protein unbound intrinsic microsomal clearance.

4. Conclusions

The master regulatory role of WEE1 kinase in cellular homeostasis has established it as an appealing biological target for cancer treatment, with the goal of developing small-molecule inhibitors of its ATP-binding pocket. Clinical studies with the previous frontrunner WEE1 inhibitor drug AZD1775 (**1**) were recently discontinued, primarily due to grade 3/4 hematological patient adverse events, which were likely a result of equipotent inhibition of PLK1 and/or on-target toxicity. In addition, only few WEE1 inhibitors are currently being evaluated clinically, with none approved by regulators. These details sparked significant interest in the development of improved WEE1 inhibitors that exhibit enhanced anticancer efficacy than **1**, that are also more selective for WEE1 over PLK1, and could ultimately be dosed at lower concentrations to potentially mitigate on-target and/or off-target toxicities.

In this study a new generation of WEE1 inhibitors were synthesized based on either clinical candidate **1** or our previous leading compound **3** (Cmpd **34**), with several analogues retaining potent WEE1 activity and many being more selective for WEE1 over PLK1. Only a few compounds showcased a translation from WEE1 potency to activity against our unique (m)CRC PDO platform, with organoid cell permeation and transporter challenges purported to be the principal reason for poor effects on cell viability. However, and gratifyingly, via SAR explorative analysis of **3**, we discovered APO-50815 (**14**, WEE1 IC_{50} value of 9 nM, PLK1 IC_{50} value of 88 nM and SI value of 10), which was slightly less selective for WEE1 than **3** (SI value of 12) but was significantly more selective than **1** (SI value of 3). APO-50815 (**14**) exhibited outstanding efficacy against the peritoneal metastatic CRC organoid lines. In brief, **14** returned IC_{50} values of 37 and 74 nM against PM003 and PM025

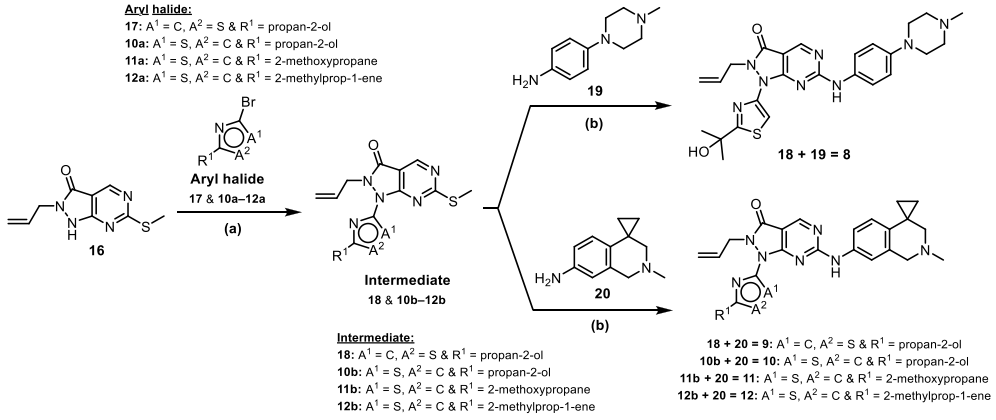

Scheme 1. Synthesis of thiazole analogues.[a]
[a]Reagents and conditions: (a) *N*,*N*′-dimethylethylenediamine, CuI, K_2CO_3, 1,4-dioxane, 95 °C, 18 h; (b) 1) *m*-CPBA/Oxone®, toluene/THF, RT, 1 h, 2) DIPEA, toluene/THF, RT, 18 h. Yield of final reactions (10–47%).

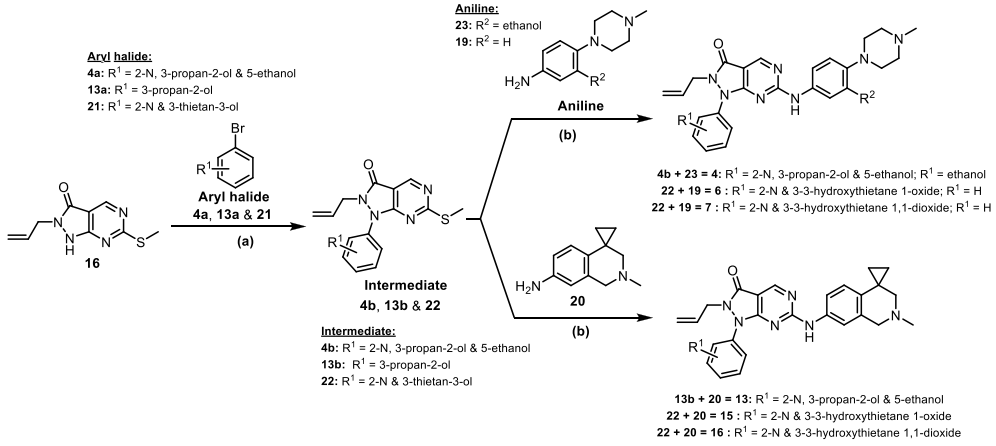

Scheme 2. Synthesis of compounds **13**, **4**–**6** and **15**–**16**.[a]
[a]Reagents and conditions: (a) *N*,*N*′-dimethylethylenediamine, CuI, K_2CO_3, 1,4-dioxane, 95 °C, 18 h; (b) 1) *m*-CPBA/Oxone®, toluene/THF, RT, 1 h, 2) DIPEA, toluene/THF, RT, 18 h. Yield of final reactions (10–85%).

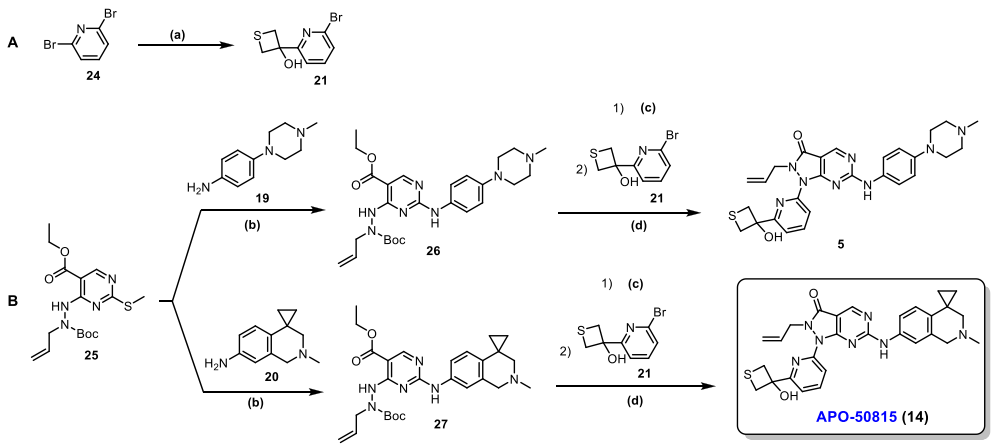

Scheme 3. Synthesis of compound **5** and APO-50815 (**14**).[a]
[a]Reagents and conditions: **A**: (a) 1) *n*-BuLi, Et_2O, −78 °C, 1 h, 2) thietane-3-one, 0 °C for 30 min then 0 °C–RT for 1 h. **B**: (b) 1) *m*-CPBA, toluene/THF, RT, 1 h, 2) DIPEA, toluene/THF, RT, 18 h. (c) 1:1 TFA:DCM, RT, ON; (d) *N*,*N*′-dimethylethylenediamine, CuI, K_2CO_3, 1,4-dioxane, 95 °C, 18 h. Yield of final reactions (51–52%).

(*TP53*-mutated peritoneal metastases), respectively. Similarly, **14** demonstrated profound efficacy against QEH039LM (*TP53*-mutated liver metastasis), returning an IC_{50} value of 55 nM. In addition, **14** demonstrated enhanced activity against the *TP53*-mutated and *KRAS*-mutated liver mCRC PDO line QEH042LM (IC_{50} value of 630 nM), which was found to be more resistant to treatment with **1** (IC_{50} value of 900 nM). Taken together, APO-50815 (**14**) exhibited superior anticancer efficacy against the metastatic CRC organoid lines of our unique PDO platform compared to our previous leading compound **3**, as well as clinical candidates **1** and ZN-c3 (**2**), which is the current best-in-class WEE1 inhibitor.

Moreover, when treating *TP53*-WT and *BRAF-V600E* primary CRC organoids (RAH051T) vs. patient-matched normal colon organoids (RAH051N), **14** exhibited strong potency against RAH051T (IC_{50} value of 39 nM) but demonstrated profoundly decreased apoptotic effects on normal colon organoid viability of RAH051N (IC_{50} value of 9300 nM). An exceptional TI value of 238 was determined, highlighting a large therapeutic window for cancer treatment. Analogously, **14** was tested against two additional patient-matched normal colon vs primary CRC organoid lines with mutated *TP53*; RAH035 and RAH057 (also with mutated *KRAS*) and returned an IC_{50} value of 6700 nM against RAH035N and 46 nM against RAH035T, with an exceptional TI value of 146. In addition, an IC_{50} value of 13000 nM against RAH057N and 101 nM against RAH057T, also with an outstanding TI value of 129. Furthermore, when treated against RAH051T, **14** was not only a stronger anticancer agent than WEE1 inhibitors **1**–**3**, but was also determined to profoundly amplify DNA damage and the frequency of cells in S phase than **1**, as well as significantly enhanced cellular apoptosis, demonstrating a broadly similar yet superior mode of action compared to **1**. Taken together, **14** was determined to be an exceptional anticancer agent against metastatic and primary CRC PDOs regardless of *TP53* mutation status or whether they have *BRAF-V600E* or mutated *KRAS*. The *in vitro* pharmacokinetic profile of **14** revealed microsomal instability that suggests further optimization would be useful in order to confer high systemic exposure. However, the negligible toxicity, DNA damage and replication stress effects to patient-matched normal colon organoids, as well as a favorable kinome-wide selectivity profile, highlight the significant and numerous attributes of **14**. Integration of matched organoids into preclinical safety studies marks a significant step forward in drug development and is a key and advantageous feature of this study.

Overall, this investigation highlights the discovery of APO-50815 (**14**), a potent and selective thietane-3-ol WEE1 inhibitor which exhibited highly selective and exceptional anticancer effects on all primary and metastatic CRC organoid lines of our unique PDO platform. Owing to its profound anticancer efficacy, APO-50815 (**14**) represents a valuable tool compound for drug testing studies against (m)CRCs, especially those using PDOs. In addition, these findings emphasize the advantage of testing anticancer agents against PDOs for fast-tracking lead compound optimization strategies compared to conventional 2D cancer cell lines. This work complements the FDA's recent initiative to reduce or phase out animal studies through replacement with PDOs and organoid-on-chip models for testing drug candidate safety and efficacy.

5. Experimental section

5.1. Computational molecular modeling

Using ICM-Pro [31] (version 3.9-4), the X-ray co-crystal structure of AZD1775 (**1**) bound within the ATP-binding pocket of WEE1 (PDB ID: 5V5Y, 1.90 Å) as the XR file was converted to an ICM object by using the 'convert to PDB' feature, in order to prepare the protein-ligand complex. Here, the default options were left untouched, but the following boxes were ticked; 'guess formal charges in ligands' and 'auto fix backbone and sidechain'. In brief, converting to an ICM object removed unbound water molecules, optimized hydrogen atoms, restored missing heavy atoms in amino acid side chains, and assigned atomic charges. Next, on the ligedit tab the 'Setup Ligand' feature was conducted at a pH of 7.4. Afterward, the 'Setup Receptor' feature was employed, with the receptor limited by a box encompassing the ligand bound to WEE1 and surrounding pocket residues. Next, the 'ligedit' feature was used for ligand modification. Pyridyl and phenyl ring modifications of **1** resulted in novel structures that were redocked and minimized to afford theoretical binding modes and their ligand-protein interactions were assessed.

5.2. In vitro biochemical kinase assays

Kinase inhibitory assays were conducted at Reaction Biology in Germany. The IC_{50} profile of the compounds were determined using at least three protein kinases (WEE1, PLK1 and CHK1). IC_{50} values were measured by testing 10 concentrations (variable concentration ranges) of each compound in duplicate or triplicate.

Sample preparation. The compounds as powders were dissolved to 100 × highest assay concentration (1 or 10 μM) in volumes of 100% DMSO. 100 μL of each of the stock solutions were transferred into column 2 of four 96 well master plates. Prior to testing, the 100 × stock solutions in column 2 of the master plates were subjected to a serial, semi-logarithmic dilution using 100% DMSO as a solvent. Subsequently, 2 × 10 μL from each well of the serial diluted copy plates were aliquoted with a 96 channel pipettor into identical sets of compound dilution

plates. In the process, 90 μL H_2O were added to each well of each compound dilution plate. To minimize potential precipitation, the H_2O was added to each plate only a few minutes before the transfer of the compound solutions into the assay plates. The plates were shaken thoroughly, resulting in compound dilution plates/10% DMSO. Several compounds were noted to have exhibited turbidity at the highest concentration(s) upon addition of water to the 100% DMSO stock solutions, indicating possible solubility issues. For the assays, 5 μL solution from each well of the compound dilution plates/10% DMSO were transferred into the assay plates. The final volume of the assay was 50 μL. All compounds were tested at 10 final assay concentrations in variable ranges. The final DMSO concentration in the reaction cocktails was 1% in all cases.

Recombinant protein kinases. All protein kinases provided by RBE were expressed in Sf9 insect cells or in *E. coli* as recombinant GST-fusion proteins or His-tagged proteins, either as full-length or enzymatically active fragments. All kinases were produced from human cDNAs and purified by either GSH-affinity chromatography or immobilized metal. Affinity tags were removed from several kinases during purification. The purity of the protein kinases was examined by SDS-PAGE/Coomassie staining, the identity was checked by mass spectroscopy.

Kinase assays. A radiometric protein kinase assay (^{33}PanQinaseTM Activity Assay) was used for measuring the kinase activity of the protein kinases. All kinase assays were performed in 96-well ScintiPlatesTM from PerkinElmer (Boston, MA, USA) in a 50 μL reaction volume. The reaction cocktail was pipetted in four steps in the following order: 25 μL of assay buffer (standard buffer/[γ-33P]-ATP), 10 μL of ATP solution (in H_2O), 5 μL of test compound (in 10% DMSO) and 10 μL of enzyme/substrate mixture. The assay for all protein kinases contained 70 mM HEPES-NaOH pH 7.5, 3 mM $MgCl_2$, 3 μM Na-orthovanadate, 1.2 mM DTT, 50 μg/mL PEG20000, ATP (variable) concentrations, corresponding to the apparent ATP-Km of the respective kinase, [γ −33P]-ATP (approx. 9 × 1005 cpm per well), protein kinase and substrate (variable amounts, see Table S1 in **Supp**.).

5.3. Patient-derived organoids

Human primary and metastatic colorectal and cancer samples were obtained at the time of surgery for routine pathological analysis. All participants gave informed written consent and research was conducted in accordance with the Declaration of Helsinki, the NHMRC Statement on Ethical Conduct in Human Research, and institutional approval (HREC/16/SAC/344 SSA/18/CALHN/71). Tumor samples were propagated as described by Narasimhan et al. [33] In brief, tissue samples were first minced and enzymatically digested in organoid digestion media containing advanced DMEM-F12 (Gibco; 12634-010), Antibiotic-Antimycotic (Gibco; 15240-062), 50 μg/mL Gentamicin (Gibco, 15750-060), 1% FCS, Collagenase IV 75 U/ml (Gibco; 17104019), Dispase 125 μg/ml (Gibco 17105-041), Hyaluronidase 20 μg/ml (Sigma; H3506), Y27632 (Sigma; Y0503) in a water bath at 37 °C for 10 min then a further 30 min shaking at 150 rpm in an orbital shaker at 37 °C. Samples were strained, washed and plated in domes of GFR-Matrigel. Human CRC organoids were cultured in colorectal cancer media containing advanced DMEM/F12 (Gibco; 12634-010), Antibiotic-Antimycotic (Gibco; 15240-062), 50 μg/ml Gentamicin (Gibco, 15750-060), 10 mM Hepes (Sigma; H0887), 1 × glutamax (Gibco; 35050-061), 2 × B27 (Gibco; 17504044), 500 nM A83–01 (Tocris; 2939), 50 ng/ml hEGF (Sigma; SRP3027), 1 nM [Leu15]-Gastrin 1 (Sigma; G9145), 1 mM N-Acetyl-Lcysteine (Sigma; A9165), 5 μM SB202190 (Sigma; S7067), 10 μM SB431542 (Sigma; S4317), and 10 μM Y27632 (Sigma; Y0503). Colorectal cancer media was changed twice weekly, with growth monitored until passaging was required.

Normal colorectal tissue samples were rocked in chelation buffer (3 mM EDTA, 50 μM DTT in PBS) for 1 h at room temperature. Crypts were released by shaking in PBS, washed and then plated in GFR-Matrigel. Human colorectal organoids were cultured in normal colorectal media containing advanced DMEM/F12 (Gibco; 12634-010), Antibiotic-Antimycotic (Gibco; 15240-062), 50 μg/ml Gentamicin (Gibco, 15750-060), 50% HUB(Wnt3a) conditioned media (as described in Lannagan et al. [38]), 20% Rspo2 conditioned media (as described in Lannagan et al. [38]), 10 mM Hepes (Sigma; H0887), 1 × glutamax (Gibco; 35050-061), 1 × B27 (Gibco; 17504044), 1 × N2 (Gibco; 17502048), 2 μM A83–01 (Tocris; 2939), 10 mM Nicotinamide (Sigma; N0636), 100 ng/ml Noggin (Peprotech AF-250-38-250), 50 ng/ml mEGF (Peprotech; 315-09-500), 10 nM [Leu15]-Gastrin 1 (Sigma; G9145), 1 mM N-Acetyl-Lcysteine (Sigma; A9165), 5 μM SB202190 (Sigma; S7067), and 10 μM Y27632 (Sigma; Y0503). Normal colorectal media was changed twice weekly, with growth monitored until passaging was required.

5.4. Immunohistochemistry (IHC)

Organoids were washed with cold PBS and fixed in 4% paraformaldehyde (Chem Cruz, sc-281692) for 1 h at room temperature. After washing extensively with PBS, organoids were suspended in warmed histogel (Thermofisher, HG-4000-012), then formalin fixed and paraffin embedded.

Formalin-fixed, paraffin-embedded (FFPE) organoid and tissue sections (4 μm) were dewaxed and stained using hematoxylin and eosin (H&E). For IHC staining, slides were subjected to sodium citrate or EDTA antigen retrieval in a steamer for 30 min before quenching endogenous peroxidase with 3% hydrogen peroxide in PBS/0.05% Tween-20 (PBS-T) for 5 min. This was followed by incubation for 1 h at room temperature with the following primary antibodies diluted in 50% protein block (DAKO, X0909) and 50% PBS-T: rabbit anti-CDX2 (1:1000 Abcam, ab76541), rabbit anti-CK20 (1:500 Abcam, ab76126), or rabbit anti-CK7 (1:100 Abcam, ab181598). After incubating with horse radish peroxidase (HRP)-conjugated secondary antibody (Goat anti-rabbit HRP, 1:1000 Abcam ab205718) for 30 min at room temperature, samples were washed and labelled with DAB kit (DAKO K3468) for 10 min. Slides were counterstained using hematoxylin.

5.5. Organoid genetic analysis

Organoid genomic DNA preparation and TP53 sequencing was conducted as in Syphers et al. [30], 2025. The primers used to amplify *KRAS* exon 2 were KRAS F:5–GGTGGAGTATTTGATAGTGTATTAACC–3 and KRAS R: 5–AGAATGGTCCTGCACCAGTAA–3 (220-bp PCR product). The primers used to amplify *BRAF* exon 15 were BRAF F 5-TCATAATGCTTGCTCTGATAGGA-3 and BRAF R 5-GGCCAAAAATTTAATCAGTGGA-3 (223-bp PCR product). Sanger sequencing was conducted by the Australian Genome Research Facility (AGRF).

5.6. Organoid compound activity testing assays

Organoids were dissociated into single cells by incubation in TrypLE (Gibco) with 10 μM Y27632 (Sigma) at 37 °C with mechanical dissociation. 1000 cells were seeded in a 5 μL GFR Matrigel (Corning) dome in white-walled 96 well plates (Corning). Solidified Matrigel domes were overlaid with 100 μL of the appropriate media. Once organoids had established (2 days post seeding), media was removed and replaced by 100 μL of drug-containing media. A 7-point 10-fold dilution series of each drug was assessed in quadruplicate. Drug concentrations ranged from 100 pM to 100 μM. Drugs were dissolved in DMSO to 1000-fold the final concentration of treatment (100 nM to 100 μM) and all treatment wells were normalized to 0.1% DMSO content. Drug-containing media was refreshed every 2-3 days for 5 days of drug treatment. Organoids were photographed (2 × lens on Olympus IX53 microscope) then cell viability was quantitated by Cell Titer Glo assay (Promega) using a GloMax microplate reader (Promega). Data analyses were performed using GraphPad Prism 7.02 software, applying nonlinear regression (curve fit) and the equation log(inhibitor) versus response - variable

slope (four parameters) to calculate IC_{50} values.

5.7. Apoptosis, DNA-damage and cell proliferation experiments

Human CRC organoids were grown for 7 days in 50 μL GFR-Matrigel domes with colorectal cancer media. 48 h before harvesting, media was replaced with 300 nM WEE1 inhibitor or vehicle (DMSO) in colorectal cancer media. Extra domes of organoids were treated with the most effective WEE1 inhibitor (APO-50815 (**14**) and AZD1775 (**1**)) for staining with each individual antibody as controls for the instrument setup. 3 h prior to harvesting, organoids were pulse labelled with 20 μM BrdU (BD Pharmingen). Organoids were dissociated into single cells by incubation in TrypLE (Gibco) with 10 μM Y27632, 2 mM EDTA and 1.5 μg/mL DNase 1 at 37 °C with mechanical dissociation. Preparation of cells and analysis was conducted according to manufacturer's instruction for the Apoptosis, DNA Damage and Cell Proliferation Kit (BD Pharmingen Cat # 562253). Controls for instrument setup included organoids stained with each individual - PerCP-Cy™5.5 Anti-BrdU (Display in Log Mode); PE Anti-Cleaved PARP (D214) (Display in Log Mode); Alexa Fluor® 647 Mouse Anti-H2AX (pS139) (Display in Log Mode) and DAPI (Display in Linear Mode). Stained cells were analyzed on BD FACS Canto II flow cytometer at a rate no greater than 400 events/sec. 3 biological replicate experiments were conducted.

5.8. Intracellular WEE1 inhibition western blot assays

Cell synchronization was performed as described by Bukhari et al. [49] A highly metastatic variant of MDA-MB-231 cell lines (3×10^5 cells, MDA-MB-231^{HM}) were seeded in a 6-well plate in DMEM supplemented with 10% FBS. The following day, cells were then treated with 2 mM thymidine for 18 h. Cells were then incubated with fresh DMEM with 10% FBS for 8 h and followed by a second incubation with 2 mM thymidine for 18 h. Cells were subsequently treated with DMSO (0.2% v/v, vehicle control) or WEE1 inhibitors (**13** and APO-50815 (**14**) at approximately $10 \times IC_{50}$ acquired from WEE1 biochemical assay). After 2 h of treatment, cells were collected in ice-cold PBS. The cell pellets were acquired after centrifugation, frozen and stored at −20 °C until further analysis.

Protein expression was determined by using Western blot. Cell pellet was lysed in RIPA buffer (1.0% Triton X-100, 0.5% sodium deoxycholate, 0.1% SDS, 150 mM NaCl, 50 mM Tris) supplemented with Complete™, Mini, EDTA-free Protease Inhibitor Cocktail (04693159001, Roche) for protein extraction. Protein concentration was determined via Bradford assay. Protein samples (20–30 μg) were then separated by a 4-15% polyacrylamide gel (4568084, Biorad) and transferred on a Immun-Blot® Low Fluorescence PVDF Membrane (1620264, Biorad) using a Trans-Blot Turbo Transfer System (Biorad). Membrane was blocked in 5% BSA in Tris-buffered saline with 0.1% Tween-20 (TBST) for 1 h. Following blocking, the membrane was incubated with primary antibodies against protein of interest at 4 °C overnight. The membrane was then washed and subsequently incubated with Alexa Fluor-conjugated secondary antibodies against specific species. Membrane was then imaged on an Amersham Typhoon 5 Imager at a resolution of 100 μm. The following antibodies were used: rabbit anti-CDK1 p-Tyr15 (4539, Cell Signalling), rabbit anti-CDK1 (77055, Cell Signalling), mouse anti-β-actin (3700, Cell Signalling), Goat anti-Rabbit IgG (H + L) Highly Cross-Adsorbed Secondary Antibody, Alexa Fluor™ 647 (21245, ThermoFisher), F(ab')2-Goat anti-Mouse IgG (H + L) Cross-Adsorbed Secondary Antibody, Alexa Fluor™ 488 (11017, ThermoFisher). The molecular weight of both CDK1 and pY15-CDK1 is around 34 kDa [31].

The acquired image was analyzed on ImageJ. The Image was first converted to an 8-bit format. A region of interest (ROI) was then created to include the protein band and mean gray value of the ROI was measured. ROI of the same size was used to measure the protein band of all the samples, including the background. The mean gray value of the background was then subtracted from the value of the protein band. The background subtracted mean gray value of pCDK1 was then normalized to that of CDK1 from the same sample. Values were then normalized to the DMSO control.

5.9. Kinome profiling

The assay was performed as previously described [50,51]. Purified proteins were buffered in 25 mM HEPES (pH 7.5), 500 mM NaCl and were assayed in a 384-wellplate with a final protein concentration of 2 μM in 10 μL assay volume. APO-50815 (**14**) was added to a final concentration of 20 μM, using an ECHO 550 acoustic dispenser (Labcyte). As a fluorescence probe, SYPRO-Orange (Molecular Probes) was added in a 1:5000 dilution. Filters for excitation and emission were set to 465 nm and 590 nm, respectively. The temperature was increased from 25 °C with 3 °C/min to a final temperature of 95 °C, while scanning, using the QuantStudio5 (Applied Biosystems). Data was analyzed through Boltzmann-equation in the Protein Thermal Shift software (Applied Biosystems). Samples were measured in technical duplicates.

5.10. In vitro microsomal metabolism studies

The metabolic stability assay was performed by incubating APO-50815 (**14**) in liver microsomes at 37 °C and a protein concentration of 0.4 mg/mL. The metabolic reaction was initiated by the addition of an NADPH regenerating system and quenched at various time points over a 60-min incubation period by the addition of MeCN containing metolazone as internal standard. Control samples (containing no NADPH) were included (and quenched at 2, 30 and 60 min) to monitor for potential degradation in the absence of co-factor. The human liver microsomes used in this experiment were supplied by XenoTech, lot #1410230. The mouse liver microsomes used in this experiment were supplied by Xeno Tech, lot #1910002. Microsomal incubations were performed at a substrate concentration of 1 μM.

Chemistry. General Material and Methods. Small molecule ^1H and ^{13}C NMR spectra were acquired at 400.13 and 100.62 MHz, respectively, on an Avance III Nanobay 400 MHz Bruker spectrometer at 298 K, coupled to the BACS 60 automatic sample changer and equipped with a 5 mm PABBO BB-1H/D Z-GRD probe. Data acquisition and processing was managed using XWINNMR (Bruker) software package version 3.5 and plotting was managed using MestReNova version 11.0.4-18998. All NMR chemical shifts (δ) were measured in parts per million (ppm) referenced to an internal standard of residual proteosolvent: chloroform-*d* (7.26 ppm for ^1H and 77.16 ppm for ^{13}C), methanol-d_4 (3.31 ppm for ^1H and 49.0 ppm for ^{13}C), DMSO-d_6 (2.50 ppm for ^1H and 39.52 ppm for ^{13}C). Solvents used for NMR studies were purchased from Cambridge Isotope Laboratories. Each proton resonance was assigned according to the following convention: chemical shift (δ), multiplicity, coupling constant (*J* Hz) and number of protons. Each carbon resonance was assigned according to the following convention: chemical shift (δ), multiplicity (where no multiplicity is assigned a singlet peak was observed), and coupling constants (*J* Hz) for carbon−fluorine coupling. Multiplicity is quoted as br (broad), s (singlet), d (doublet), t (triplet), q (quartet), p (pentet), and m (multiplet).

Analysis by LRMS was performed in Agilent 6120 Series Single Quadrupole LCMS coupled with an Agilent 1260 Infinity series ultra-HPLC, a 1200 series G1312B quaternary pump, a 1260 series G1367E HiP ALS autosampler, and a 1290 series G4212A photodiode array detector. Acquisition and analysis were performed using the Chemstation software Rev.B.04.03 coupled with Mass Hunter Easy Access. The conditions for liquid chromatography were: column, Agilent Poroshell 120 EC-C18 2.7 μm (3 mm × 500 mm) 120 Å; column temperature: 35 °C; injection volume: 1 μL; solvent A: 0.1% formic acid in ultrapure H_2O; solvent B: 0.1% formic acid in MeCN; flow rate: 0.5 mL/min; gradient: 5−100% of solvent B over 2.5 min, maintained for a further 3.8 min; detection: 254 nm and 214 nm. The conditions for mass

spectrometry were: quadrupole ion source; ion mode: API-ES; drying gas temp: 350 °C; vaporizer temperature: 200 °C; capillary voltage: 3000 V (positive and negative); scan range: 100−1000 *m/z*; step size: 0.1 s; acquisition time: 5 min.

HRMS analyses were acquired on an Agilent 6224 TOF LCMS Mass Spectrometer coupled to an Agilent 1290 Infinity series ultra HPLC. All data were acquired, and reference mass corrected via a dual-spray electrospray ionization (ESI) source. Each scan or data point on the Total Ion Chromatogram (TIC) is an average of 13,700 transients, producing a spectrum every second. Mass spectra were created by averaging the scans across each peak and background subtracted against the first 10 s of the TIC. Acquisition was performed using the Agilent Mass Hunter Data Acquisition software version B.05.00 Build 5.0.5042.2 and analysis was performed using Mass Hunter Qualitative Analysis Version B.05.00 Build 5.0.519.13. The conditions for mass spectrometry were ion mode: ESI; drying gas flow: 11 L/min; nebulizer: 45 psi; drying gas temperature: 325 °C; capillary voltage: 4000 V; fragmentor (160 V), skimmer (65 V); octupole RFV (750 V), scan range: 100−1500 *m/z*; internal reference ions: positive ion mode = *m/z* = 121.050873 and 922.009798. The conditions for liquid chromatography were reversed-Phase HPLC analysis fitted with an Agilent Zorbax SB-C18 Rapid Resolution HT 1.8 μm (2.1 mm × 50 mm) 80 Å column; solvent A: 0.1% formic acid in ultrapure H_2O; solvent B: 0.1% formic acid in MeCN; flow rate: 0.5 mL/min; gradient: 5−100% of solvent B over 3.5 min.

All assayed compounds are >95% pure by analytical HPLC. Compound purity was determined using an Agilent 1260 Infinity Analytical HPLC (1260 Infinity G1322A Degasser, 1260 Infinity G1312B Binary pump, G1367E HiP ALS autosampler, 1260 Infinity G1316A Thermostatted Column Compartment, and 1260 Infinity G4212B DAD detector). The conditions for liquid chromatography were: column, Agilent Zorbax Eclipse Plus C18 Rapid Resolution 3.5 μm (4.6 mm × 100 mm) 95 Å; column temperature: 35 °C; injection volume: 1 μL; solvent A: 0.1% trifluoroacetic acid (TFA) in ultrapure H_2O; solvent B: 0.1% TFA in MeCN; flow rate: 1.0 mL/min; gradient: 5−100% of solvent B over 9 min, maintained for a further 1 min; detection: 254 and 214 nm.

5.11. General procedures

5.11.1. General procedure A: Ullman-type reaction

N,*N*′-Dimethylethylene-diamine (2.0 equiv.) was added to a solution of 2-allyl-6-(methylthio)-1,2-dihydro-3*H*-pyrazolo[3,4-*d*]pyrimidin-3-one **16** (1.0 equiv.), the relevant aryl halide (1.3 equiv.), copper iodide (2.5 equiv.) and K_2CO_3 (1.4 equiv.) in 1,4-dioxane (2 mL/mmol) at 80 °C. The resultant suspension was heated at 95 °C for 18 h, over which in time a color change of orange to dark green or dark brown occurred. After completion, the reaction mixture was cooled to RT and diluted with NH_4OH (1 mL/mmol) before being extracted with EtOAc (2 × 5 mL/mmol). The combined organic extracts were washed with brine (1 mL/mmol), dried ($MgSO_4$) and evaporated to dryness before the crude material was purified by chromatography on silica to afford the desired products (68–71%).

5.11.2. General procedure B: Two-step coupling using an oxidant

m-CPBA or Oxone® (3.0 equiv.) was added to a solution of the relevant intermediate pyrimidinylpyrazolone (1.0 equiv.) in THF/toluene (2 mL/mmol) for *m*-CPBA or THF:H_2O (3:1, 2 mL/mmol) for Oxone®, and the resulting mixture was stirred at RT for 1 h. DIPEA (3.0 equiv.) and the relevant substituted aniline or amine (1.3 equiv.) were added, and the reaction mixture was stirred at RT for 18 h. Sat. $NaHCO_3$ solution (2 mL/mmol) was added, and the mixture was extracted with EtOAc (2 × 4 mL/mmol). The combined organic extracts were washed with brine (1 mL/mmol), dried ($MgSO_4$) and concentrated *in vacuo*. The resultant residues were purified by chromatography on silica to afford the target compounds (24–82%).

5.11.2.1. 2-Allyl-6-((3-(hydroxymethyl)-4-(4-methylpiperazin-1-yl) phenyl)amino)-1-(4-(hydroxymethyl)-6-(2-hydroxypropan-2-yl)pyridin-2-yl)-1,2-dihydro-3H-pyrazolo[3,4-d]pyrimidin-3-one (4).

The title compound was prepared according to general procedure B. Orange solid (71 mg, 0.13 mmol, 85%); **^{1}H NMR** (401 MHz, Acetone-d_6) δ 8.77 (s, 1H), 8.04 (d, J = 8.2 Hz, 1H), 7.92 – 7.84 (m, 1H), 7.71 – 7.60 (m, 2H), 7.39 (d, J = 8.6 Hz, 1H), 5.72 (ddt, J = 16.5, 10.3, 6.1 Hz, 1H), 5.00 (dd, J = 10.2, 1.3 Hz, 1H), 4.90 (m, 1H), 4.84 (s, 2H), 4.81 – 4.75 (m, 2H), 4.73 (s, 2H), 3.69 (d, J = 11.4 Hz, 2H), 3.61 – 3.47 (m, 2H), 3.44 – 3.32 (m, 2H), 3.29 – 3.21 (m, 1H), 3.02 (s, 3H), 1.55 (s, 6H); **^{13}C NMR** (101 MHz, Acetone-d_6) δ 167.0, 155.4, 154.8, 147.7, 145.0, 137.7, 135.9, 132.3, 121.0, 120.4, 120.3, 118.9, 118.0, 117.96, 117.94, 113.9, 113.3, 107.8, 72.5, 62.5, 60.0, 54.0, 49.6, 46.9, 42.5, 30.1; **HRMS** (APCI): *m/z* calculated for $C_{29}H_{37}N_8O_4$ $[M+H]^+$: 561.2932, found: 561.2946.

5.11.2.2. 2-Allyl-1-(6-(3-hydroxythietan-3-yl)pyridin-2-yl)-6-((4-(4-methylpiperazin-1-yl)phenyl)amino)-1,2-dihydro-3H-pyrazolo[3,4-d]pyrimidin-3-one (5).

The title compound was prepared according to general procedure B. Yellow solid (22 mg, 0.041 mmol, 51%); **^{1}H NMR** (401 MHz, Acetone-d_6) δ 8.79 (s, 1H), 8.02 (t, J = 7.9 Hz, 1H), 7.91 (d, J = 8.1 Hz, 1H), 7.81 (d, J = 8.6 Hz, 2H), 7.72–7.65 (m, 1H), 7.08 (d, J = 8.7 Hz, 2H), 5.75 (dd, J = 16.3, 7.4 Hz, 1H), 5.09–5.00 (m, 4H), 3.90–3.66 (m, 6H), 3.65–3.59 (m, 2H), 3.40–3.17 (m, 4H), 3.03 (s, 3H); **^{13}C NMR** (101 MHz, Acetone-d_6) δ 163.0, 155.5, 154.2, 153.8, 151.2, 150.2, 148.4, 147.1, 141.6, 140.1, 133.0, 131.8, 122.6, 122.4, 120.5, 117.9, 117.1, 116.7, 79.4, 53.9, 51.4, 47.6, 43.3, 41.3.

5.11.2.3. 2-Allyl-1-(6-(3-hydroxy-1-oxidothietan-3-yl)pyridin-2-yl)-6-((4-(4-methylpiperazin-1-yl)phenyl)amino)-1,2-dihydro-3H-pyrazolo[3,4-d]pyrimidin-3-one (6).

The title compound was prepared according to general procedure B. Yellow solid (14 mg, 0.026 mmol, 31%); **^{1}H NMR** (401 MHz, DMSO-d_6) δ 10.19 (s, 1H), 8.84 (s, 1H), 8.09 (d, J = 9.1 Hz, 1H), 7.81 (d, J = 8.1 Hz, 1H), 7.59–7.51 (m, 3H), 7.15 (s, 1H), 6.93 (d, J = 8.7 Hz, 2H), 5.67 (ddt, J = 17.2, 10.3, 5.9 Hz, 1H), 5.05–4.97 (m, 1H), 4.89 (dd, J = 17.1, 1.4 Hz, 1H), 4.67 (d, J = 5.9 Hz, 2H), 4.21–4.13 (m, 2H), 3.54–3.46 (m, 2H), 3.13 (t, J = 4.9 Hz, 4H), 2.55 (s, 4H), 2.29 (s, 3H); **^{13}C NMR** (101 MHz, DMSO-d_6) δ 162.7, 161.6, 161.0, 156.1, 147.7, 147.4, 147.0, 139.3, 132.1, 130.8, 121.3, 121. 2, 118.3, 116.6, 116.1, 115.5, 67.7, 67.3, 54.4, 48.2, 46.8, 45.4, 30.7, 26.8; **LCMS** (ESI+) *m/z* = 547.2 $[M + H]^+$.

5.11.2.4. 2-Allyl-1-(6-(3-hydroxy-1,1-dioxidothietan-3-yl)pyridin-2-yl)-6-((4-(4-methylpiperazin-1-yl)phenyl)amino)-1,2-dihydro-3H-pyrazolo [3,4-d]pyrimidin-3-one (7).

The title compound was prepared according to general procedure B. Yellow solid (3 mg, 0.0053 mmol, 10%); **^{1}H NMR** (401 MHz, DMSO-d_6) δ 10.19 (s, 1H), 8.84 (s, 1H), 8.09 (d, J = 9.1 Hz, 1H), 7.81 (d, J = 8.1 Hz, 1H), 7.59–7.51 (m, 3H), 7.15 (s, 1H), 6.93 (d, J = 8.7 Hz, 2H), 5.67 (ddt, J = 17.2, 10.3, 5.9 Hz, 1H), 5.05–4.97 (m, 1H), 4.89 (dd, J = 17.1, 1.4 Hz, 1H), 4.67 (d, J = 5.9 Hz, 2H), 4.41–4.37 (m, 2H), 3.81–3.76 (m, 2H), 3.17–3.13 (m, 4H), 2.61–2.56 (m, 4H), 2.30 (s, 3H); **LCMS** (ESI+) *m/z* = 563.1 $[M + H]^+$.

5.11.2.5. 2-Allyl-1-(2-(2-hydroxypropan-2-yl)thiazol-4-yl)-6-((4-(4-methylpiperazin-1-yl)phenyl)amino)-1,2-dihydro-3H-pyrazolo[3,4-d]pyrimidin-3-one (8).

The title compound was prepared according to general procedure B. Yellow solid (30 mg, 0.060 mmol, 43%); **^{1}H NMR** (400 MHz, Chloroform-*d*) δ 8.79 (s, 1H), 7.65 (s, 1H), 7.47–7.35 (m, 3H), 6.88 (d, J = 8.5 Hz, 2H), 5.72 (ddt, J = 16.5, 11.0, 6.0 Hz, 1H), 5.11–4.96 (m, 2H), 4.62 (d, J = 6.1 Hz, 2H), 3.18 (t_{app}, J = 4.9 Hz, 4H), 2.58 (t_{app}, J = 4.9 Hz, 4H), 2.35 (s, 3H), 1.70 (s, 6H); **^{13}C NMR** (101 MHz, Chloroform-*d*) δ 178.2, 176.1, 171.9, 166.9, 162.6, 161.4, 161.3, 159.3, 156.3, 153.9, 144.1, 136.9, 131.9, 130.7, 118.9, 116.6, 73.8, 55.2, 49.6, 47.1, 46.3, 30.9; **LCMS** (ESI+) *m/z* = 507.2 $[M + H]^+$.

*5.11.2.6. 2-Allyl-1-(2-(2-hydroxypropan-2-yl)thiazol-4-yl)-6-((2′-methyl-2′,3′-dihydro-1′H-spiro[cyclopropane-1,4′-isoquinolin]-7′-yl)amino)-1,2-dihydro-3H-pyrazolo[3,4-d]pyrimidin-3-one (**9**).* The title compound was prepared according to general procedure B. Yellow solid (21 mg, 0.043 mmol, 25%); **^{1}H NMR** (400 MHz, DMSO-d_6) δ 10.80 (s, 1H), 10.31 (s, 1H), 8.89 (s, 1H), 7.89 (s, 1H), 7.60 (s, 1H), 7.53 (d, J = 8.4 Hz, 1H), 6.77 (d, J = 8.6 Hz, 1H), 6.20 (s, 1H), 5.69 (ddt, J = 16.1, 10.8, 5.6 Hz, 1H), 5.10–5.02 (m, 1H), 5.00–4.90 (m, 1H), 4.49–4.23 (m, 4H), 3.26 (s, 2H), 2.84 (s, 3H), 1.51 (s, 6H), 1.25–1.23 (m, 2H), 1.09–1.06 (m, 2H); **^{13}C NMR** (101 MHz, DMSO-d_6) δ 181.0, 161.1, 159.7, 155.9, 142.8, 142.8, 137.2, 132.1, 130.8, 128.8, 121.9, 120.1, 118.0, 117.9, 117.1, 97.9, 72.2, 58.2, 54.8, 45.6, 41.7, 30.7, 30.5, 16.0; **LCMS** (ESI+) m/z = 504.2 $[M + H]^+$.

*5.11.2.7. 2-Allyl-1-(4-(2-hydroxypropan-2-yl)thiazol-2-yl)-6-((2′-methyl-2′,3′-dihydro-1′H-spiro[cyclopropane-1,4′-isoquinolin]-7′-yl)amino)-1,2-dihydro-3H-pyrazolo[3,4-d]pyrimidin-3-one (**10**).* The title compound was prepared according to general procedure B. Yellow solid (4 mg, 0.0079 mmol, 10%); **^{1}H NMR** (400 MHz, Methanol-d_4) δ 8.77 (s, 1H), 7.54 (s, 1H), 7.44 (s, 1H), 7.41–7.34 (m, 1H), 6.63 (d, J = 8.6 Hz, 1H), 5.68 (ddt, J = 16.4, 10.2, 5.9 Hz, 1H), 5.09–5.02 (m, 1H), 5.02–4.92 (m, 1H), 4.52 (d, J = 6.0 Hz, 2H), 4.29 (s, 2H), 3.24 (s, 2H), 2.93 (s, 3H), 1.61 (s, 6H), 1.19–1.04 (m, 4H); **LCMS** (ESI+) m/z = 504.2 $[M + H]^+$.

*5.11.2.8. 2-Allyl-1-(4-(2-methoxypropan-2-yl)thiazol-2-yl)-6-((2′-methyl-2′,3′-dihydro-1′H-spiro[cyclopropane-1,4′-isoquinolin]-7′-yl)amino)-1,2-dihydro-3H-pyrazolo[3,4-d]pyrimidin-3-one (**11**).* The title compound was prepared according to general procedure B. Yellow solid (3 mg, 0.0058 mmol, 15%); **^{1}H NMR** (600 MHz, DMSO-d_6) δ 10.51 (s, 1H), 9.21 – 8.82 (m, 1H), 8.03–7.88 (m, 1H), 7.66–7.45 (m, 2H), 6.79–6.65 (m, 1H), 5.72 (s, 1H), 5.15–4.97 (m, 1H), 4.90 (s, 1H), 3.69–3.54 (m, 2H), 3.12–2.97 (m, 2H), 2.48–2.39 (m, 3H), 2.37–2.30 (m, 3H), 1.54–1.50 (m, 3H), 0.99–0.80 (m, 4H); **LCMS** (ESI+) m/z = 518.2 $[M + H]^+$.

*5.11.2.9. 2-Allyl-6-((2′-methyl-2′,3′-dihydro-1′H-spiro[cyclopropane-1,4′-isoquinolin]-7′-yl)amino)-1-(4-(prop-1-en-2-yl)thiazol-2-yl)-1,2-dihydro-3H-pyrazolo[3,4-d]pyrimidin-3-one (**12**).* The title compound was prepared according to general procedure B. Yellow solid (10 mg, 0.021 mmol, 47%); **^{1}H NMR** (400 MHz, DMSO-d_6) δ 10.52 (s, 1H), 8.92 (s, 1H), 7.62 (s, 1H), 7.53 (s, 1H), 7.46 (dd, J = 8.5, 2.3 Hz, 1H), 6.72 (d, J = 8.5 Hz, 1H), 5.86 (d, J = 2.3 Hz, 1H), 5.74 (ddt, J = 16.5, 10.2, 6.0 Hz, 1H), 5.22 (t, J = 1.9 Hz, 1H), 5.08 (dd, J = 10.2, 1.5 Hz, 1H), 5.02 (dd, J = 17.1, 1.6 Hz, 1H), 4.92 (d, J = 6.1 Hz, 2H), 3.61 (s, 2H), 2.47 (s, 2H), 2.34 (s, 3H), 2.09 (s, 3H), 0.95–0.90 (m, 2H), 0.88–0.84 (m, 2H); **^{13}C NMR** (101 MHz, DMSO-d_6) δ 162.3, 161.0, 160.1, 156.5, 151.0, 136.5, 135.2, 134.8, 134.5, 131.9, 121.6, 119.5, 118.9, 117.9, 114.2, 111.6, 62.4, 58.5, 54.9, 48.6, 45.1, 30.7, 19.8, 18.6, 17.1.

*5.11.2.10. 2-Allyl-1-(3-(2-hydroxypropan-2-yl)phenyl)-6-((2′-methyl-2′,3′-dihydro-1′H-spiro[cyclopropane-1,4′-isoquinolin]-7′-yl)amino)-1,2-dihydro-3H-pyrazolo[3,4-d]pyrimidin-3-one (**13**).* The title compound was prepared according to general procedure B. White solid (30 mg, 0.060 mmol, 51%); **^{1}H NMR** (400 MHz, Acetone-d_6) δ 9.05 (s, 1H), 8.72 (s, 1H), 7.65–7.46 (m, 5H), 7.43 (d, J = 7.6 Hz, 1H), 6.66 (d, J = 8.4 Hz, 1H), 5.73 (ddt, J = 17.3, 10.3, 5.9 Hz, 1H), 5.07 (dd, J = 10.2, 1.3 Hz, 1H), 4.98 (dd, J = 17.1, 1.5 Hz, 1H), 4.34 (dd, J = 6.2, 1.6 Hz, 2H), 3.54 (s, 2H), 2.46 (s, 2H), 2.35 (s, 3H), 1.56 (s, 6H), 0.94–0.87 (m, 2H), 0.87–0.81 (m, 2H); **^{13}C NMR** (101 MHz, Acetone-d_6) δ 168.7, 163.9, 163.1, 162.7, 162.6, 158.4, 156.5, 153.3, 137.4, 137.3, 136.3, 134.9, 132.8, 129.7, 124.9, 124.2, 122.4, 119.6, 118.9, 72.0, 64.1, 60.0, 46.9, 45.9, 32.4, 19.5, 17.6; **LCMS** (ESI+) m/z = 497.2; **HRMS** (APCI): m/z calculated for $C_{29}H_{32}N_6O_2$ $[M+H]^+$: 497.2660, found: 497.2652.

*5.11.2.11. 2-Allyl-1-(6-(3-hydroxythietan-3-yl)pyridin-2-yl)-6-((2′-methyl-2′,3′-dihydro-1′H-spiro[cyclopropane-1,4′-isoquinolin]-7′-yl)amino)-1,2-dihydro-3H-pyrazolo[3,4-d]pyrimidin-3-one (**14**, **APO-50815**).* The title compound was prepared according to general procedure B. White solid (30 mg, 0.060 mmol, 52%); **^{1}H NMR** (400 MHz, Acetone-d_6) δ 8.79 (s, 1H), 8.13 (t, J = 7.9 Hz, 1H), 7.98 (dd, J = 8.1, 0.9 Hz, 1H), 7.79–7.69 (m, 1H), 7.61 (s, 1H), 7.43 (dd, J = 8.5, 2.3 Hz, 1H), 6.72 (d, J = 8.5 Hz, 1H), 5.75 (ddt, J = 16.6, 10.2, 6.2 Hz, 1H), 5.04–4.93 (m, 2H), 4.91 (dt, J = 6.2, 1.4 Hz, 2H), 3.80–3.72 (m, 2H), 3.66 (s, 2H), 3.63–3.54 (m, 2H), 2.52 (s, 2H), 2.40 (s, 3H), 1.00–0.92 (m, 2H), 0.92–0.85 (m, 2H); **^{13}C NMR** (101 MHz, Acetone-d_6) δ 163.5, 162.6, 162.5, 162.0, 156.9, 148.8, 141.5, 140.2, 137.0, 136.0, 135.2, 133.2, 122.5, 120.1, 119.0, 118.6, 118.2, 117.9, 79.4, 63.8, 59.9, 48.0, 45.7, 41.2, 19.4, 17.7; **HPLC** – t_R = 7.40 min > 95% purity at 254 nm; **LCMS** (ESI+) m/z = 528.2; **HRMS** (APCI): m/z calculated for $C_{28}H_{29}N_7O_2S$ $[M+H]^+$: 528.2176, found: 528.2171.

*5.11.2.12. 2-Allyl-1-(6-(3-hydroxy-1-oxidothietan-3-yl)pyridin-2-yl)-6-((2′-methyl-2′,3′-dihydro-1′H-spiro[cyclopropane-1,4′-isoquinolin]-7′-yl)amino)-1,2-dihydro-3H-pyrazolo[3,4-d]pyrimidin-3-one (**15**).* The title compound was prepared according to general procedure B. White solid (30 mg, 0.060 mmol, 31%); **^{1}H NMR** (400 MHz, DMSO-d_6) δ 10.33 (s, 1H), 8.90 (s, 1H), 8.11 (t, J = 7.2 Hz, 1H), 7.83 (d, J = 8.0 Hz, 1H), 7.57 (d, J = 7.5 Hz, 2H), 7.42 (d, J = 7.4 Hz, 1H), 7.22 (s, 1H), 6.74 (d, J = 8.2 Hz, 1H), 5.76–5.59 (m, 1H), 5.01 (d, J = 9.9 Hz, 1H), 4.89 (d, J = 17.2 Hz, 1H), 4.72–4.64 (m, 2H), 4.18 (d, J = 10.9 Hz, 2H), 3.91 (s, 2H), 3.52 (d, J = 10.3 Hz, 2H), 2.79 (s, 2H), 2.56 (s, 3H), 1.01–0.92 (m, 4H); **^{13}C NMR** (101 MHz, DMSO-d_6) δ 162.8, 161.3, 161.0, 160.7, 156.2, 147.6, 139.3, 135.8, 134.7, 133.9, 132.0, 121.4, 119.0, 118.3, 117.2, 116.8, 116.3, 67.7, 67.3, 62.4, 58.6, 46.6, 45.1, 30.7, 18.6, 17.0; **LCMS** (ESI+) m/z = 544.2.

*5.11.2.13. 2-Allyl-1-(6-(3-hydroxy-1,1-dioxidothietan-3-yl)pyridin-2-yl)-6-((2′-methyl-2′,3′-dihydro-1′H-spiro[cyclopropane-1,4′-isoquinolin]-7′-yl)amino)-1,2-dihydro-3H-pyrazolo[3,4-d]pyrimidin-3-one (**16**).* The title compound was prepared according to general procedure B. White solid (30 mg, 0.060 mmol, 42%); **^{1}H NMR** (400 MHz, DMSO-d_6) δ 10.30 (s, 1H), 8.91 (d, J = 7.5 Hz, 1H), 8.31–8.23 (m, 1H), 8.03 (dd, J = 11.8, 8.1 Hz, 1H), 7.60–7.45 (m, 1H), 7.37 (t, J = 9.4 Hz, 1H), 6.91 (s, 1H), 6.69 (dd, J = 8.5, 3.6 Hz, 1H), 5.72 (s, 1H), 5.72–5.62 (m, 1H), 5.02 (dd, J = 9.4, 5.9 Hz, 1H), 4.97–4.86 (m, 1H), 4.76 (d, J = 5.9 Hz, 1H), 4.62 (d, J = 5.7 Hz, 1H), 3.57 (d, J = 4.3 Hz, 2H), 3.09–3.04 (m, 2H), 2.46 (s, 2H), 2.35 (s, 3H), 1.28–1.20 (m, 2H), 0.91 (s, 2H), 0.84 (s, 2H). **^{13}C NMR** (101 MHz, DMSO-d_6) δ 161.4, 161.0, 156.4, 156.3, 151.0, 150.0, 140.1, 139.8, 135.9, 135.8, 133.8, 132.1, 121.6, 119.9, 119.0, 118.5, 90.9, 62.3, 58.4, 45.0, 44.3, 42.0, 30.7, 26.8, 18.5, 17.0; **LCMS** (ESI+) m/z = 560.2.

CRediT authorship contribution statement

Joel L. Syphers: Formal analysis, Investigation, Methodology, Software, Validation, Visualization, Writing – original draft, Writing – review & editing. **Josephine A. Wright:** Data curation, Formal analysis, Methodology, Writing – original draft, Writing – review & editing. **Rebekah de Nys:** Data curation, Formal analysis. **Tharindie N. Silva:** Investigation, Methodology. **Laura Vrbanac:** Investigation, Methodology. **Kate R. Barratt:** Investigation, Methodology. **Julia Leeflang:** Investigation, Methodology. **Sadia T. Hasan:** Investigation, Methodology. **Sophie F. Thomson:** Investigation, Methodology. **Adarsh Kumar:** Data curation, Formal analysis, Investigation, Methodology. **Andreas Krämer:** Investigation, Methodology. **Christopher Lenz:** Data curation, Formal analysis, Investigation, Methodology. **Yi Sing Gee:** Investigation, Methodology. **Aeson Chang:** Investigation, Methodology, Writing – original draft. **Savannah Young:** Data curation, Methodology. **Erica K. Sloan:** Investigation, Methodology, Supervision, Writing – original draft, Writing – review & editing. **Stefan Knapp:** Data curation, Resources, Supervision. **Daniel L. Worthley:** Formal analysis, Supervision.

Siddhartha Mukherjee: Conceptualization, Supervision. **Kieran Stockton:** Data curation, Formal analysis, Investigation, Writing – original draft. **Daniel L. Priebbenow:** Data curation, Formal analysis, Investigation, Resources, Supervision, Writing – original draft, Writing – review & editing. **Susan L. Woods:** Conceptualization, Data curation, Formal analysis, Funding acquisition, Investigation, Methodology, Supervision, Validation, Visualization, Writing – original draft, Writing – review & editing. **Jonathan B. Baell:** Conceptualization, Formal analysis, Funding acquisition, Investigation, Methodology, Project administration, Resources, Supervision, Validation, Writing – original draft, Writing – review & editing.

Declaration of competing interest

The authors declare that they have no known competing financial interests or personal relationships that could have appeared to influence the work reported in this paper.

Acknowledgments

This work was funded by grants from National Health and Medical Research Council (*APP1156391* to D.L. Worthley, and S.L. Woods) and The Gastroenterological Society of Australia Bushell Research Fellowship (S.L.W.), the Faculty of Health Science at the University of Adelaide (S.L.W), the South Australian Health and Medical Research Institute (S.L.W.). S.K, A.K and C.L are grateful for support from the Structural Genomics Consortium (SGC), a registered charity (no: 1097737) that receives funds from Bristol Myers Squibb, Genome Canada through Ontario Genomics Institute, EU/EFPIA/OICR/McGill/KTH/Diamond Innovative Medicines Initiative 2 Joint Undertaking [EUbOPEN grant 875510], Janssen, Pfizer, and Takeda. SK is also funded by the German Cancer Research Center (DKTK), the Frankfurt Cancer Institute (FCI) and S.K and A.K are funded by the German Cancer Aid (Krebshilfe) preclinical drug development program TACTIC. J.L.S. was supported by an Australian Government Research Training Program Scholarship and a Monash Graduate Excellence Scholarship provided by Monash University. The author(s) acknowledge the facilities, and the scientific and technical assistance of the Australian Translational Medicinal Chemistry Facility (ATMCF), Monash Institute of Pharmaceutical Sciences (MIPS). ATMCF is supported by Therapeutic Innovation Australia (TIA). TIA is supported by the Australian Government through the National Collaborative Research Infrastructure Strategy (NCRIS) program. Fig. 1 was created with BioRender.com (*created in BioRender. Syphers, J. (2025)* https://BioRender.com/d2a3iv4). Fig. 4A was created with BioRender.com (*created in BioRender. Woods, S. (2025)* https://BioRender.com/0x316ec).

Appendix A. Supplementary data

Supplementary data to this article can be found online at https://doi.org/10.1016/j.ejmech.2026.118838.

ABBREVIATIONS USED

ATM, ataxia telangiectasia mutated kinase; ATR; ataxia telangiectasia and Rad-3-related kinase; CDC2, cell division cycle 2; CDC25, cell division cycle 25; CDK1/2, cyclic-dependent kinases 1 and 2; CHK1, checkpoint kinase 1; Cmpd, compound; DDRC, DNA-damage repair checkpoint; DNA, deoxyribonucleic acid; HBD, hydrogen bond donor; IPA, isopropyl alcohol; mets, metastases; mCRC, metastatic colorectal cancer; N/A, not available; PDOs, patient-derived organoids; PKMYT1, membrane-associated tyrosine- and threonine-specific CDC2-inhibitory kinase; p, phosphorylated; PLK1, polo-like kinase 1; p53, tumor suppressor protein p53; SD, standard deviation; THIQ, tetrahydroisoquinoline; WT, wild type; y/o, years old; 2D, two-dimensional; 3D, three-dimensional.

Data availability

All data is included in the SI.

References

[1] G. Milletti, V. Colicchia, F. Cecconi, Cyclers' kinases in cell division: from molecules to cancer therapy, Cell Death Differ. 30 (9) (2023) 2035–2052.
[2] S.-B. Koh, The expanding role of WEE1, Cell. Signal. 94 (2022) 110310.
[3] T. Otto, P. Sicinski, Cell cycle proteins as promising targets in cancer therapy, Nat. Rev. Cancer 17 (2) (2017) 93–115.
[4] K. Do, J.H. Doroshow, S. Kummar, Wee1 kinase as a target for cancer therapy, Cell Cycle 12 (19) (2013) 3348–3353.
[5] A. Stathis, A. Oza, Targeting Wee1-like protein kinase to treat cancer, Drug News Perspect. 23 (7) (2010) 425–429.
[6] R.C. Jackson, The DNA damage checkpoint. Evolutionary Dynamics of Malignancy: the Genetic and Environmental Causes of Cancer, 2023, pp. 65–83.
[7] H. Chen, F. Yang, Q. Zhao, H. Wang, M. Zhu, H. Li, Z. Ge, S. Zhang, Q. Guo, H. Hui, GL-V9 synergizes with oxaliplatin of colorectal cancer via Wee1 degradation mediated by HSP90 inhibition, J. Pharm. Pharmacol. (2024) rgae060.
[8] H. Beck, V. Nähse-Kumpf, M.S.Y. Larsen, K.A. O'Hanlon, S. Patzke, C. Holmberg, J. Mejlvang, A. Groth, O. Nielsen, R.G. Syljuåsen, C.S. Sørensen, Cyclin-dependent kinase suppression by WEE1 kinase protects the genome through control of replication initiation and nucleotide consumption, Mol. Cell Biol. 32 (20) (2012) 4226–4236.
[9] C.R. Elbæk, V. Petrosius, J. Benada, L. Erichsen, R.B. Damgaard, C.S. Sørensen, WEE1 kinase protects the stability of stalled DNA replication forks by limiting CDK2 activity, Cell Rep. 38 (3) (2022).
[10] T. Schutte, A. Embaby, N. Steeghs, S. van der Mierden, W. van Driel, M. Rijlaarsdam, A. Huitema, F. Opdam, Clinical development of WEE1 inhibitors in gynecological cancers: a systematic review, Cancer Treat Rev. 115 (2023) 102531.
[11] H. Hirai, Y. Iwasawa, M. Okada, T. Arai, T. Nishibata, M. Kobayashi, T. Kimura, N. Kaneko, J. Ohtani, K. Yamanaka, H. Itadani, I. Takahashi-Suzuki, K. Fukasawa, H. Oki, T. Nambu, J. Jiang, T. Sakai, H. Arakawa, T. Sakamoto, T. Sagara, T. Yoshizumi, S. Mizuarai, H. Kotani, Small-molecule inhibition of Wee1 kinase by MK-1775 selectively sensitizes p53-deficient tumor cells to DNA-damaging agents, Mol. Cancer Therapeut. 8 (11) (2009) 2992–3000.
[12] B. Vogelstein, D. Lane, A.J. Levine, Surfing the p53 network, Nature 408 (6810) (2000) 307–310.
[13] L. Heinst, K.S. Lee, R. Berthold, I. Isfort, S. Wosnig, A. Kuntze, S. Hafner, B. Altvater, C. Rössig, P. Åman, E. Wardelmann, C. Scholl, W. Hartmann, S. Fröhling, M. Trautmann, Exploiting WEE1 kinase activity as FUS::DDIT3-dependent therapeutic vulnerability in myxoid liposarcoma, bioRxiv 2024 (03.13) (2024) 584771.
[14] A.A.B.A. da Costa, D. Chowdhury, G.I. Shapiro, A.D. D'Andrea, P. A. Konstantinopoulos, Targeting replication stress in cancer therapy, Nat. Rev. Drug Discov. 22 (1) (2023) 38–58.
[15] D. Chen, X. Lin, J. Gao, L. Shen, Z. Li, B. Dong, C. Zhang, X. Zhang, Wee1 inhibitor AZD1775 combined with Cisplatin potentiates anticancer activity against gastric cancer by increasing DNA damage and cell apoptosis, BioMed Res. Int. 2018 (2018), 2018), No. 5813292.
[16] C.J. Matheson, S. Venkataraman, V. Amani, P.S. Harris, D.S. Backos, A.M. Donson, M.F. Wempe, N.K. Foreman, R. Vibhakar, P. Reigan, A WEE1 inhibitor analog of AZD1775 maintains synergy with Cisplatin and demonstrates reduced single-agent cytotoxicity in medulloblastoma cells, ACS Chem. Biol. 11 (7) (2016) 2066–2067.
[17] C.J. Matheson, K.A. Casalvieri, D.S. Backos, P. Reigan, Development of potent Pyrazolopyrimidinone-Based WEE1 inhibitors with limited single-agent cytotoxicity for cancer therapy, ChemMedChem 13 (16) (2018) 1681–1694.
[18] G. Wright, V. Golubeva, L.L. Remsing Rix, N. Berndt, Y. Luo, G.A. Ward, J.E. Gray, E. Schonbrunn, H.R. Lawrence, A.N.A. Monteiro, U. Rix, Dual targeting of WEE1 and PLK1 by AZD1775 elicits single agent cellular anticancer activity, ACS Chem. Biol. 12 (7) (2017) 1883–1892.
[19] C. Zhang, K. Peng, Q. Liu, Q. Huang, T. Liu, Adavosertib and beyond: biomarkers, drug combination and toxicity of WEE1 inhibitors, Crit. Rev. Oncol. Hematol. 193 (2024) 104233.
[20] P. Ye, Z. Zhang, D. Zhang, M. Zhang, M. Wang, P. Cai, Y. Huang, Y. Song, PLK1 inhibitors for the treatment of colorectal cancer, Ann. Med. Surg. 87 (7) (2025) 4165–4172.
[21] A.M. Zeidan, M. Ridinger, T.L. Lin, P.S. Becker, G.J. Schiller, P.A. Patel, A.I. Spira, M.L. Tsai, E. Samuëlsz, S.L. Silberman, M. Erlander, E.S. Wang, A phase Ib study of Onvansertib, a novel oral PLK1 inhibitor, in combination therapy for patients with relapsed or refractory acute Myeloid leukemia, Clin. Cancer Res. 26 (23) (2020) 6132–6140.
[22] D. Olmos, D. Barker, R. Sharma, A.T. Brunetto, T.A. Yap, A.B. Taegtmeyer, J. Barriuso, H. Medani, Y.Y. Degenhardt, A.J. Allred, D.A. Smith, S.C. Murray, T. A. Lampkin, M.M. Dar, R. Wilson, J.S. de Bono, S.P. Blagden, Phase I study of GSK461364, a specific and competitive Polo-like kinase 1 inhibitor, in patients with advanced solid malignancies, Clin. Cancer Res. 17 (10) (2011) 3420–3430.
[23] P. Schöffski, A. Awada, H. Dumez, T. Gil, S. Bartholomeus, P. Wolter, M. Taton, H. Fritsch, P. Glomb, G. Munzert, A phase I, dose-escalation study of the novel Polo-like kinase inhibitor volasertib (BI 6727) in patients with advanced solid tumours, Eur. J. Cancer 48 (2) (2012) 179–186.
[24] S. Guler, M.C. DiPoto, A. Crespo, R. Caldwell, B. Doerfel, N. Grossmann, K. Ho, B. Huck, C.C.V. Jones, R. Lan, D. Musil, J. Potnick, H. Schilke, B. Sherer, S. Simon,

C. Sirrenberg, Z. Zhang, L. Liu-Bujalski, Selective Wee1 inhibitors led to antitumor activity in vitro and correlated with myelosuppression, ACS Med. Chem. Lett. 14 (5) (2023) 566–576.
[25] J.F. Seligmann, D.J. Fisher, L.C. Brown, R.A. Adams, J. Graham, P. Quirke, S. D. Richman, R. Butler, E. Domingo, A. Blake, E. Yates, M. Braun, F. Collinson, R. Jones, E. Brown, E. de Winton, T.C. Humphrey, M. Parmar, R. Kaplan, R. H. Wilson, M. Seymour, T.S. Maughan, Inhibition of WEE1 is effective in TP53- and RAS-Mutant metastatic colorectal cancer: a randomized trial (FOCUS4-C) comparing adavosertib (AZD1775) with active monitoring, J. Clin. Oncol. 39 (33) (2021) 3705–3715.
[26] P.Q. Huang, B.C. Boren, S.G. Hegde, H. Liu, A.K. Unni, S. Abraham, C.D. Hopkins, S. Paliwal, A.A. Samatar, J. Li, K.D. Bunker, Discovery of ZN-c3, a highly potent and selective Wee1 inhibitor undergoing evaluation in clinical trials for the treatment of cancer, J. Med. Chem. 64 (17) (2021) 13004–13024.
[27] Azenosertib clinical trials pipeline. https://www.zentalis.com/pipeline/pipeline#azenosertib (accessed December 22, 2025).
[28] A Phase 1/2, Open-Label, Multi-Center Study of ZN-c3 Administered in Combination with Encorafenib and Cetuximab in Adults with Metastatic Colorectal Cancer. in Pfizer, Ed, 2023.
[29] V.J. Alli, P. Yadav, V. Suresh, S.S. Jadav, Synthetic and medicinal chemistry approaches toward WEE1 kinase inhibitors and its degraders, ACS Omega 8 (23) (2023) 20196–20223.
[30] J.L. Syphers, J.A. Wright, S. Liu, Y.S. Gee, F. Gao, R. Mudududdla, D.Q. Che, A. Chang, E.K. Sloan, V. Narasimhan, A. Heriot, R.G. Ramsay, R. de Nys, T.N. Silva, L. Vrbanac, T. Sammour, M.J. Lawrence, T. Tin, G.J. Maddern, K. Fenix, H. Kaur, K. Barratt, G. Kelter, A. Maier, M. Posch, H. Lu, X. Wang, A. Zhavoronkov, H. Wei, F. Huang, D.L. Worthley, D.L. Priebbenow, S. Mukherjee, S.L. Woods, J.B. Baell, Discovery of WEE1 kinase inhibitors with potent activity against patient-derived, metastatic colorectal cancer organoids, J. Med. Chem. 68 (8) (2025) 8065–8090.
[31] R. Abagyan, M. Totrov, D. Kuznetsov, ICM—A new method for protein modeling and design: applications to docking and structure prediction from the distorted native conformation, J. Comput. Chem. 15 (5) (1994) 488–506.
[32] Y. Wang, C. Xu, Y. Jiang, Z. Tu, J. Yan, L. Guo, C. Dong, J. Liu, X. Yang, Z. Wang, T. Lu, J. Feng, Y. Chen, Advanced design, synthesis, and evaluation of highly selective Wee1 inhibitors: enhancing pharmacokinetics and antitumor efficacy, J. Med. Chem. 67 (12) (2024) 9927–9949.
[33] V. Narasimhan, J.A. Wright, M. Churchill, T. Wang, R. Rosati, T.R.M. Lannagan, L. Vrbanac, A.B. Richardson, H. Kobayashi, T. Price, G.X.Y. Tye, J. Marker, P. J. Hewett, M.P. Flood, S. Pereira, G.A. Whitney, M. Michael, J. Tie, S. Mukherjee, C. Grandori, A.G. Heriot, D.L. Worthley, R.G. Ramsay, S.L. Woods, Medium-throughput drug screening of patient-derived organoids from colorectal peritoneal metastases to direct personalized therapy, Clin. Cancer Res. 26 (14) (2020) 3662–3670.
[34] Y.J. Kim, C.H. Kim, Treatment for peritoneal metastasis of patients with colorectal cancer, Ann. Coloproctol 37 (6) (2021) 425–433.
[35] H. Zhou, Z. Liu, Y. Wang, X. Wen, E.H. Amador, L. Yuan, X. Ran, L. Xiong, Y. Ran, W. Chen, Y. Wen, Colorectal liver metastasis: molecular mechanism and interventional therapy, Signal Transduct. Targeted Ther. 7 (1) (2022). No. 70.
[36] D. Tuveson, H. Clevers, Cancer modeling meets human organoid technology, Science 364 (6444) (2019) 952–955.
[37] L. Memeo, V. Canzonieri, F. Rizzolio, Cancer organoids in basic science and translational medicine, Cancers (Basel) 13 (15) (2021). No. 3701.
[38] T.R.M. Lannagan, Y.K. Lee, T. Wang, J. Roper, M.L. Bettington, L. Fennell, L. Vrbanac, L. Jonavicius, R. Somashekar, K. Gieniec, M. Yang, J.Q. Ng, N. Suzuki, M. Ichinose, J.A. Wright, H. Kobayashi, T.L. Putoczki, Y. Hayakawa, S.J. Leedham, H.E. Abud, H. Yilmaz Ö, J. Marker, S. Klebe, P. Wirapati, S. Mukherjee, S. Tejpar, B.A. Leggett, V.L.J. Whitehall, D.L. Worthley, S.L. Woods, Genetic editing of colonic organoids provides a molecularly distinct and orthotopic preclinical model of serrated carcinogenesis, Gut 68 (4) (2019) 684–692.
[39] D. Wang, R. Villenave, N. Stokar-Regenscheit, H. Clevers, Human organoids as 3D in vitro platforms for drug discovery: opportunities and challenges, Nat. Rev. Drug Discov. (2025).
[40] U.S. Food, A. Drug, FDA Announces Plan to Phase out Animal Testing Requirement for Monoclonal Antibodies and Other Drugs, FDA Press Announcements, 2025.
[41] M. Ariyoshi, R. Yuge, Y. Kitadai, D. Shimizu, R. Miyamoto, K. Yamashita, Y. Hiyama, H. Takigawa, Y. Urabe, S. Oka, WEE1 inhibitor adavosertib exerts antitumor effects on colorectal cancer, especially in cases with p53 mutations, Cancers (Basel) 16 (18) (2024). No. 3136.
[42] J.L. Syphers, J.A. Wright, A. Kumar, N. To, L. Elson, A. Krämer, S. Müller, V. Morasch, A. Chang, S. Young, E.K. Sloan, R. de Nys, T.N. Silva, L. Vrbanac, K. R Barratt, J. Leeflang, S.T. Hasan, R.W. Gable, S. Knapp, D.L. Worthley, S. Mukherjee, K. Stockton, S.L. Woods, D.L. Priebbenow, J.B. Baell, Selective Macrocyclic WEE1 Kinase Inhibitors with Strong Efficacy Against Patient-Derived Colorectal Cancer Organoids. *Manuscript in Preparation*, 2026.
[43] C.A. Lipinski, F. Lombardo, B.W. Dominy, P.J. Feeney, Experimental and computational approaches to estimate solubility and permeability in drug discovery and development settings, Adv. Drug Deliv. Rev. 23 (1) (1997) 3–25.
[44] A. Mateus, L.J. Gordon, G.J. Wayne, H. Almqvist, H. Axelsson, B. Seashore-Ludlow, A. Treyer, P. Matsson, T. Lundbäck, A. West, M.M. Hann, P. Artursson, Prediction of intracellular exposure bridges the gap between target- and cell-based drug discovery, Proc. Natl. Acad. Sci. USA. 114 (30) (2017) E6231–E6239.
[45] K.S. Prabhu, S. Kuttikrishnan, N. Ahmad, U. Habeeba, Z. Mariyam, M. Suleman, A. A. Bhat, S. Uddin, H2AX: a key player in DNA damage response and a promising target for cancer therapy, Biomed. Pharmacother. 175 (2024) 116663.
[46] F.J. Groelly, M. Fawkes, R.A. Dagg, A.N. Blackford, M. Tarsounas, Targeting DNA damage response pathways in cancer, Nat. Rev. Cancer 23 (2) (2023) 78–94.
[47] C.N. Johnstone, A.D. Pattison, K.L. Gorringe, P.F. Harrison, D.R. Powell, P. Lock, D. Baloyan, M. Ernst, A.G. Stewart, T.H. Beilharz, R.L. Anderson, Functional and genomic characterisation of a xenograft model system for the study of metastasis in triple-negative breast cancer, Dis. Model. Mech. 11 (5) (2018).
[48] T. Jin, W. Xu, R. Chen, L. Shen, J. Gao, L. Xu, X. Chi, N. Lin, L. Zhou, Z. Shen, B. Zhang, Discovery of potential WEE1 inhibitors via hybrid virtual screening, Front. Pharmacol. 14 (2023) 1298245.
[49] A.B. Bukhari, C.W. Lewis, J.J. Pearce, D. Luong, G.K. Chan, A.M. Gamper, Inhibiting Wee1 and ATR kinases produces tumor-selective synthetic lethality and suppresses metastasis, J. Clin. Investig. 129 (3) (2019) 1329–1344.
[50] O. Fedorov, F.H. Niesen, S. Knapp, Kinase inhibitor selectivity profiling using differential scanning fluorimetry, Methods Mol. Biol. 795 (2012) 109–118.
[51] A. Krämer, C.G. Kurz, B.T. Berger, I.E. Celik, A. Tjaden, F.A. Greco, S. Knapp, T. Hanke, Optimization of pyrazolo[1,5-a]pyrimidines lead to the identification of a highly selective casein kinase 2 inhibitor, Eur. J. Med. Chem. 208 (2020) 112770.